Effects of Varying Saturation Vapor Pressure on Climate, Clouds, and Convection®

FRANCISCO E. SPAULDING-ASTUDILLO^a AND JONATHAN L. MITCHELL^{a,b}

^a Department of Earth, Planetary, and Space Sciences, University of California, Los Angeles, Los Angeles, California ^b Department of Atmospheric and Oceanic Sciences, University of California, Los Angeles, Los Angeles, California

(Manuscript received 22 March 2022, in final form 29 January 2023, accepted 3 February 2023)

ABSTRACT: We investigate how climate, clouds, and convection change as the amount of water vapor in the atmosphere is varied by altering the saturation vapor pressure (SVP) by a constant in a one-dimensional climate model. We identify four effects of altering SVP on clouds in an Earthlike climate with distinct layers of low and high clouds. First, the anvils of high clouds get higher as SVP is increased (and vice versa) because they are bound by radiative constraints to occur at a lower temperature. The vapor pressure path above the cold anvils does not change in Earthlike climates. Second, low clouds get lower as SVP increases (and vice versa) because they are coupled to a convective boundary layer (CBL) that shallows primarily from an increase in the tropospheric static stability. The third and fourth effects follow from the first two, namely, that single-layer cloud states exist both in vapor-poor states with a merged cloud deck and vapor-rich states with an elevated cloud deck. We identify two cloud instability parameters that determine the transitions between single-and double-layer cloud regimes. Qualitatively, sufficiently vapor-poor states have a deep, diffusive layer that overlaps with a weaker convective layer (topping out at the tropopause) that cannot maintain low relative humidity in the midtroposphere through the drying of descending air, thus causing the cloud layers to merge. Sufficiently vapor-rich states lose their low clouds as the shallowing CBL drops below the lifting condensation level.

KEYWORDS: Convection; Boundary layer; Clouds; Climate change; Cloud radiative effects; Water vapor

1. Introduction

Water vapor is essential to all aspects of Earth's climate, clouds, and convection. This is most obvious, perhaps, in Earth's tropics where to good approximation a balance is struck between radiative cooling and condensational heating (O'Gorman et al. 2012). Water vapor is not only a latent source of energy, but it also controls the flow of radiation to space, as water is the strongest gaseous emitter of infrared radiation in Earth's troposphere (Harrop and Hartmann 2012). Clear-sky radiative cooling generates convective motions that, in turn, control the vertical distribution of water vapor and thereby the cloud distribution (Hartmann and Larson 2002). In regions of high relative humidity, water vapor readily condenses into clouds (Slingo 1980), introducing competing shortwave and longwave cloud radiative effects. Because its density is less than that of dry air at the same temperature, water vapor in sufficient, near-surface abundance is also a trigger of convection (Yang and Seidel 2020). If the atmosphere has much more or much less water vapor, any and all of these processes are affected. This is evident in, for instance, the latitudinal variations in Earth's cloud phenomenology (Sassen and Wang 2008).

Titan, Saturn's largest moon, has an active weather cycle involving evaporation and condensation of methane, and offers

© Supplemental information related to this paper is available at the Journals Online website: https://doi.org/10.1175/JAS-D-22-0063.s1.

Corresponding author: Francisco E. Spaulding-Astudillo, fspauldinga@ucla.edu

the only present-day point of comparison with Earth's weather. Like water, methane is a greenhouse gas with a positive climate feedback, transports heat horizontally and vertically, and triggers moist convection that is associated with precipitation and cloud formation (Mitchell and Lora 2016). In other ways, Earth and Titan are quite distinct. Take, for example, the volatility of their condensables, which we define as the vapor pressure of water at Earth's conditions and that of methane at Titan's conditions. There is ~100 times more precipitable methane in Titan's atmosphere (\sim 5 m) than water in Earth's (\sim 5 cm) (Tokano et al. 2006; Hartmann 2016). At the same time, Titan is weakly irradiated and far colder than Earth. Titan's atmosphere is optically thick at most infrared wavelengths, which along with frigid conditions (~70-90 K) makes it challenging for the atmosphere to cool radiatively. Perhaps because of this, deep convection on Titan appears to be much rarer than on Earth (Lorenz et al. 2005) and clouds cover <1% of Titan's global surface area, compared to almost 70% of Earth's in the annual mean (Griffith et al. 2000; King et al. 2013).

The rarity of clouds and deep convection on Titan could be due to a number of other effects, for example, the differences in the microphysics of methane and water cloud formation. A fruitful approach to studying these differences is to develop separate weather/climate models for Earth and Titan (Rafkin et al. 2022; Lora et al. 2015). Adapting Earth climate and weather models to Titan necessarily involves changing many components simultaneously, which can obscure the causes behind any differences. In addition, the interesting physics that distinguish climate, clouds, and convection on Earth and Titan may occur in the parameter space between the two, where a climate tipping point or "regime change" occurs. An idealized experiment that accesses the parameter space between

DOI: 10.1175/JAS-D-22-0063.1

^{© 2023} American Meteorological Society. For information regarding reuse of this content and general copyright information, consult the AMS Copyright Policy (www.ametsoc.org/PUBSReuseLicenses).

the end members is needed to identify whether a climate regime change is present.

Motivated by this, we ask a simple question: What would Earth's climate, clouds, and convection be like if water vapor were much more (or less) abundant? And relatedly, are there sharp regime changes (tipping points) in the equilibrium climate states? We carry out a numerical experiment varying a single parameter that controls water vapor abundance with a one-dimensional climate model built with the column physics of the ECHAM6 GCM (Popp et al. 2015, henceforth P15). A scaling parameter for the saturation vapor pressure (SVP) put forward in a series of papers studying water vapor's role in an idealized GCM (Frierson et al. 2006, 2007),

$$e_{\text{sat}} = \xi e_{\text{sat}}^*(T), \tag{1}$$

is varied over states that are vapor poor ($\xi < 1$) and vapor rich ($\xi > 1$), where $e_{\rm sat}$ and $e_{\rm sat}^*$ are the altered and true SVP, respectively. The use of a 1D model facilitates the exploration of a wide parameter space, but comes at the expense of a number of approximations and parameterizations. Our goal with this paper is to identify the climate regime changes and understand their behavior in 1D. We intend to follow up with a three-dimensional cloud-resolving model (CRM) in future work to test our findings.

Many other studies are focused on understanding the response of an Earthlike climate to significant changes in surface temperature due to some climate forcing, e.g., large changes in nonvolatile greenhouse gases (Caballero and Huber 2010; Schneider et al. 2019, henceforth S19) or changes in sunlight (Wolf and Toon 2015; P15). Our work is complementary, in that we independently vary Earth's volatile greenhouse gas (which can be regarded as a hypothetical climate forcing). We thus expect the effect of water vapor on the climate to be more clearly identifiable in our approach. We might also expect to find the same climate states as in P15, for instance, and their presence in our experiments would provide some validation of our approach.

This paper is structured as follows: In section 2, we develop four hypotheses about the response of clouds to variations in moisture. In section 3, we describe the climate model used in this study and our experimental method. In section 4, we give an overview of our results and we evaluate our hypotheses. We characterize 3 cloudy climate states that emerge and explain the underlying cause of each climate transition with the help of two cloud-instability parameters. In section 5, we discuss our results and compare them to previous work. Finally, in section 6, we summarize our main conclusions.

2. How do climate, clouds, and convection respond to changing ξ?

Earth's tropics are characterized by several distinct cloud populations in the vertical (Johnson et al. 1999). The two dominant modes in cloud fraction are located in the lower and upper troposphere (e.g., see Fig. 1 from Seeley et al. 2019a), respectively, which we will refer to as low clouds and high clouds. Each mode consists of multiple cloud types. The

main low cloud types are cumulus (Cu) and stratocumulus (Sc) (Cesana et al. 2019; Albrecht et al. 2019; Johnson et al. 1999), which cool the climate by increasing the planetary albedo. An important way in which Cu and Sc are differentiated is by their fractional area coverage. Sc often form in sheets with a high area coverage that promotes strong radiative cooling from the cloud top (Wood 2012), producing a turbulent circulation that couples the cloud layer to its source of moisture near the surface (Stevens 2006). In contrast, Cu have moderate cloud fractions because the individual clouds are horizontally scattered. Surface heating primarily drives the turbulent circulation that resupplies moisture to Cu (Cesana et al. 2019). Whether conditions favor Sc or Cu depends on numerous factors. For instance, Sc (Cu) are more common over cold (warm) sea surface temperatures (SST) (Cesana et al. 2019). Where SSTs spatially vary, transitions between the main low cloud types naturally occur (Albrecht et al. 2019), for example, from Sc to Cu or vice versa. The main high cloud type is cumulonimbus (Johnson et al. 1999). A peak in detrainment is observed in the upper troposphere as a result of these deep convective clouds (Johnson et al. 1999), which are associated with convergence of cloudy air into clear-sky regions (Seeley et al. 2019a). The spreading anvils produce tropical cirrus that then persist for hundreds of kilometers away from the convective tower (Sokol and Hartmann 2020; Sassen et al. 2009) and warm the climate by a greenhouse effect. In this study, we use a single-column GCM that through the parameterizations described in section 3 produces low clouds and high (cirrus-like) clouds in simulations of Earth's present climate.

As we have pointed out, low clouds and high (cirrus-like) clouds have opposite effects on climate and are well separated vertically, but need they be? And are the two modes always present? We develop four hypotheses aimed at answering these questions. In section 2a, we form the first hypothesis—high clouds get higher as SVP increases—by making an assumption about anvil temperatures in altered climates. In section 2b, we form the second hypothesis—low clouds get lower as SVP increases—by considering how the height of a cloudtopped convective boundary layer depends on ξ . In section 2c, we form a third hypothesis—there exist vapor-poor states with single-layer clouds—that emerges intuitively from the first two. Finally, in section 2d, we form a fourth hypothesis there exist vapor-rich states with single-layer clouds—by considering an important constraint on low cloud formation. Later, in section 4, we will test how varying water vapor through ξ affects the basic physics that account for the existence and vertical separation of low and high clouds in an atmospheric column.

a. Hypothesis 1: High clouds get higher

We hypothesize that high clouds get higher in more vaporrich states. Our hypothesis is based on the fixed anvil temperature (FAT) hypothesis put forward by Hartmann and Larson (2002). FAT links the decreases in longwave cooling near the tropopause to the height of the convective anvil clouds (Seeley et al. 2019b). Jeevanjee and Fueglistaler (2020, henceforth

JF20b) recently showed that longwave cooling can be approximated as direct cooling-to-space from optical depth unity $(\tau_{\tilde{\nu}}=1)$ surfaces integrated over all wavenumbers $\tilde{\nu}$ in the water vapor rotational band. The spectrally integrated cooling rate is effectively the product of three parts: 1) Planck's law, 2) an emissivity gradient that depends on the thermodynamic state of the atmosphere, and 3) a spectral width that represents how many wavenumbers contribute to the total emission at each height. The key finding of JF20b is that part 3 controls the height where the cooling rate decreases because part 1 and part 2 cancel out over much of the troposphere. JF20b identified that at lower pressures fewer wavenumbers contribute to the spectrally integrated cooling rate and this causes the cooling rate to drop. The drop happens at a characteristic value of the spectral absorption coefficient $\kappa_{\rm ref}$.

Interestingly, the theory of JF20b predicts that radiative cooling decreases at a fixed vapor pressure path (VPP = $\int_0^p e \, dp$, where e is the partial pressure of water vapor and p is the total air pressure). The dependence of the cooling rate on VPP is covered in detail by Hartmann et al. (2022):

$$VPP = \frac{g p_{ref}}{D \varepsilon \kappa_{ref}} \approx 1.2 \times 10^4 \text{ Pa Pa}_v, \tag{2}$$

where D=1.66 is the two-stream diffusivity factor, ε is the ratio of the specific gas constants of dry air and water vapor, g is gravity, and $\kappa_{\rm ref}=40~{\rm m}^2~{\rm kg}^{-1}$ is the absorption coefficient at which cooling rates are expected to drop (JF20b). JF20b obtain their absorption coefficient distribution from a reference pressure of $p_{\rm ref}=500~{\rm hPa}$. Equation (2) is obtained by setting the spectrally resolved optical depth to unity at $\kappa_{\rm ref}$ and solving for VPP. For those interested, a full derivation of Eq. (2) is provided in the online supplementary material of this paper. The units of VPP are pressure of air (Pa) times partial pressure of water vapor (Pa_v). Note that Eq. (2) depends only on fixed spectroscopic and thermodynamic properties of water vapor.

Our ξ experiment perturbs the thermodynamic state of the atmosphere, but has no effect on the spectral properties of water vapor (which constrain the VPP). Therefore, we expect that the VPP where the clear-sky longwave cooling rate decreases and the high cloud forms should not vary as ξ increases. If this constraint holds, we expect that increasing ξ requires the cloud pressure to decrease to offset the moisture increase at each height. We also expect that the cloud temperature decreases with increasing ξ . If the cloud forms at roughly the same vapor pressure as we move from ξ_1 to ξ_2 where $\xi_1 < \xi_2$, then by this assumption $\xi_1 e_{\text{sat}}(T_1) = \xi_2 e_{\text{sat}}(T_2)$ and therefore $T_2 < T_1$. If both the cloud temperature and environmental lapse rate decrease, then the cloud should rise. In complementary work, Harrop and Hartmann (2012) vary the radiative effect of water vapor in the upper troposphere by specifying the water vapor amount fed into their model's radiative transfer scheme. When the partial pressure of water vapor was increased, the cloud maximum moved upward to a lower temperature.

b. Hypothesis 2: Low clouds get lower

Heating of the surface by shortwave absorption generates turbulence that sustains Cu clouds. From prior work (e.g., Fig. 2 from P15) and knowledge of the shallow convection scheme (Tiedtke 1989) in the 1D GCM used in this study (ECHAM6), one confidently expects the low-level clouds in 1D simulations of the present-day climate to fall into a Cu-like regime. We assume that the simulated low clouds are coupled to the convective boundary layer (CBL) and, therefore, that their heights are coupled. Based on this assumption, we derive an equation for the equilibrium height of a cumulus-topped CBL from the model of Neggers et al. (2006, henceforth N06) and then develop a hypothesis regarding how ξ changes the height of the low clouds.

For an isolated column in which there is no large-scale mass transport, the cumulus-topped boundary layer height h (in m), depends on the entrainment mass flux E (in m s⁻¹), and the convective mass flux M (in m s⁻¹) at the top of the boundary layer:

$$\frac{\partial h}{\partial t} = E - M. \tag{3}$$

Given expressions for E and M, one can solve for the h in steady state, E = M, where E represents the change in boundary layer height from turbulent entrainment of free-tropospheric air and M represents the change in boundary layer height from the loss of air that reaches the LCL in rising thermals and is made positively buoyant by the release of latent heat. The entrainment mass flux is

$$E = \frac{-\overline{w'\Theta_v'}|_h}{\Delta\Theta_v} = \frac{0.2\overline{w'\Theta_v'}|_s}{\Delta\Theta_v},\tag{4}$$

where $\overline{w'\Theta_v'}|_h$ and $\overline{w'\Theta_v'}|_s$ are the eddy heat fluxes at h and the surface, respectively, w' and Θ_v' are the vertical velocity and virtual potential temperature anomalies of buoyant plumes, and $\Delta\Theta_v$ is the moist tropospheric stability, which is proportional to the difference in virtual potential temperature between the boundary layer and the free troposphere. In CBLs, $\overline{w'\Theta_v'}|_h$ is of opposite sign and proportional to $\overline{w'\Theta_v'}|_s$ by a factor of 0.2 (Driedonks and Tennekes 1984), which we assume is independent of ξ . $\overline{w'\Theta_v'}|_s$ can be written in terms of the surface turbulent fluxes (Deardorff 1972),

$$\overline{w'\Theta_{v}'}|_{s} = \frac{\overline{SH}}{\rho c_{p}} + 0.61\Theta|_{s} \frac{\overline{LH}}{\rho L_{v}}, \tag{5}$$

where $\overline{\rm SH}$ and $\overline{\rm LH}$ are the sensible and latent heat fluxes at the surface (in W m⁻²), L_v is the latent heat of vaporization, c_p is the specific heat of dry air, ρ is the air density, and $\Theta|_s$ is the potential temperature at the surface. The Δ symbol preceding a variable denotes a difference between its average value in the boundary layer and the overlying free troposphere:

$$\Delta\Theta_v = \Delta\Theta + 0.61\Delta(q\Theta),$$
 (6a)

$$\Delta\Theta = C_{\Theta}^{h}(\Theta^{FT} - \Theta^{BL}), \tag{6b}$$

$$\Delta(q\Theta) = C_{\Theta}^{h}(q^{\text{FT}}\Theta^{\text{FT}} - q^{\text{BL}}\Theta^{\text{BL}}), \tag{6c}$$

$$\Delta q = C_a^h(q^{\rm FT} - q^{\rm BL}),\tag{6d}$$

where Θ is potential temperature, q is specific humidity, and $C_{\Theta}^h = 0.03$ and $C_q^h = 0.1$ are empirical transfer coefficients from the large-eddy simulations of N06, which we assume to be independent of ξ . Variables with the superscripts of "BL" or "FT" are pressure-weighted averages over the boundary layer or free troposphere, respectively. The value of M is obtained by multiplying the convective velocity w^* by the convective area fraction a_c :

$$M = a_* w^*, \tag{7}$$

where $w^* = [(gh/\Theta_v)\overline{w'\Theta_v'}|_s]^{1/3}$ is the typical vertical velocity of eddies in the CBL. a_c is the fraction of eddies that reach the LCL and then leave the boundary layer and is parameterized following Neggers et al. (N06; Neggers et al. 2007) (see section 4c). Combining Eqs. (4)–(7) and setting E = M,

$$h_{\text{cbl}} = \left(\frac{0.2}{a_c \Delta \Theta_v}\right)^3 (\overline{w' \Theta_v'}|_s)^2 \frac{\Theta_v|_s}{g}.$$
 (8)

Note that this is an implicit equation for $h_{\rm cbl}$ because a_c is a function of the CBL height. It is evaluated numerically by iterating over a series of guesses for $h_{\rm cbl}$ and finding where the equality holds within an acceptable margin of error (we arbitrarily choose ± 1 m).

It is not obvious how Eq. (8) should vary as ξ increases. Mathematically, one reasonably expects that the terms raised to higher exponents will dominate Eq. (8). Assuming that this is the case, we focus on a_c and $\Delta\Theta_v$. We are unable to offer a simple explanation for how a_c will change, as this depends on the boundary layer turbulence, which has never been studied in varying- ξ experiments. $\Delta\Theta_{\nu}$, on the other hand, is a measure of the static stability of the atmosphere, which was found by Frierson et al. (2006) to increase with increasing ξ . The static stability is given by the vertical gradient in potential temperature. Through the effect of moist convection as ξ increases, the environmental lapse rate will relax toward a smaller moist adiabatic lapse rate, and thus enhance the static stability. An increase in tropospheric stability would curb the entrainment of free-tropospheric air into the boundary layer as given by Eq. (4), and would, in turn, cause the CBL to shallow (N06; Wood 2012). Furthermore, Frierson et al. (2006) found that at low ξ the troposphere essentially becomes a dry boundary layer, indicating that turbulence is increasingly restricted near the surface with increasing ξ . The implication is that low clouds could get lower if they remain coupled to the CBL. Therefore, we hypothesize that low clouds get lower in response to increases in tropospheric stability. We acknowledge that this hypothesis may be incorrect if the other terms in Eq. (8) dominate unexpectedly. In section 4c, we will evaluate Eq. (8) using the data from our varying- ξ experiments and compare it to the depth of the simulated boundary layer.

Hypothesis 3: There exist vapor-poor states with single-layer clouds

In section 2a, we hypothesized that high clouds get lower as ξ decreases (and vice versa) if they obey the basic physics behind the FAT hypothesis (Hartmann and Larson 2002). This

is in part because the cloud temperature should increase as ξ decreases. In addition, the environmental lapse rate should steadily converge on the dry adiabatic lapse rate as ξ decreases. Combining the high cloud temperature change with the lapse rate change, the implication is that high clouds should get lower with decreasing ξ . We can only expect a decrease in high cloud height with decreasing ξ up to a point: latent heat release in convective motions as $\xi \to 0$ will become negligible and here the physics behind the FAT hypothesis breaks down. In section 2b, we hypothesized that low clouds get higher as ξ decreases (and vice versa) if the decrease in tropospheric stability (associated with the lapse rate change) facilitates more boundary layer entrainment and deepens the CBL. If both hypotheses are correct, there will be less separation between cloud layers as the atmosphere becomes more vapor poor. Moreover, the top of the boundary layer is likely to reach the tropopause in the most vapor-poor states (Frierson et al. 2006). It follows that the high and low cloud layers could merge as the atmosphere becomes more vapor poor. We thus hypothesize that there exist single-layer clouds in some vaporpoor states.

d. Hypothesis 4: There exist vapor-rich states with single-layer clouds

We hypothesize that increases in atmospheric moisture lead to a low cloud breakup event. In a series of papers, Popp et al. (P15; Popp et al. 2016) showed that the transition from an Earthlike climate with two-layer clouds to a moist greenhouse¹ climate with elevated, single-layer clouds is facilitated not only by increases in insolation but also by increases in the concentration of greenhouse gases. The climate transition is triggered by the breakup of low clouds. Here, we explore a pathway for low clouds to break up that has not been considered elsewhere: namely, if hypothesis 2 is correct, then it follows that the LCL may eventually come to lie outside of the shallowing CBL. In this scenario, moist surface parcels no longer reach the height where they can condense, precluding cloud formation altogether. Thus, we hypothesize that the breakup of low clouds in more vapor-rich atmospheres is due to the CBL moving below the LCL.

3. Model and method

We now test the four hypotheses in climate simulations with varying ξ . We use a version of the ECHAM6 climate model in single-column mode with modifications where water is allowed to be a major constituent (P15; Stevens et al. 2013). We run full-sky simulations at a time step of 180 s using the default setup from P15 with one exception. We include a seasonal cycle to make the control simulation as Earthlike as possible. Since our focus is on the equilibrium climate of the simulations, we temporally average the data (unless otherwise

¹ The moist greenhouse is a warm climate state found in multiple studies that is more proximal to the modern-day Earth climate than the runaway greenhouse, and within which surface liquids are thermodynamically stable and the cold trap at the tropopause is weakened, allowing water vapor to seep into the stratosphere.

specified) over the last 5 years to remove seasonal and annual biases. We leave it to future work to quantify the effect of seasonality on the simulated clouds. In the simulations, we alter the volatility of water vapor by multiplying the true SVP of water by the parameter ξ as shown in Eq. (1).

The simulations begin in the year 2001 and are run almost 200 years. The column is located at 38°N, where the average annual insolation is equal to the global mean. The surface is a mixed layer ocean with a fixed depth of 50 m, an initial temperature of 289 K, and an albedo of 0.07. The surface temperature is determined prognostically. We use an Earthlike solar constant of 1360 W m⁻², an obliquity of 23.4°, and zero eccentricity. Water vapor and cloud condensates are determined prognostically. Greenhouse gas concentrations are specified from a climatological distribution that extends from the preindustrial to the year 2500. $CO_2 = 550$ ppmv, $CH_4 = 1550$ ppbv, $N_2O = 380$ ppby, CFC-11 = 10 ppty, and CFC-12 = 100 ppty have uniform volume mixing ratios; only the concentrations of CH₄ and N₂O decay above the tropopause. The concentrations cited above are reached roughly by the year 2125, and are fixed at these levels until the end of the simulation. In each simulation year, the vertical profile of O₃ is set to a monthly averaged CMIP5 climatology of the year 2000. The atmospheric column is resolved into 95 vertical layers. Radiative transfer is carried out by the Rapid Radiative Transfer Model for General Circulation Models (RRTMG) (Iacono et al. 2008). ECHAM6 resolves the shortwave and longwave into 14 and 16 bands, respectively, and accounts for changes in water vapor and clouds in the radiation calculation.

Cloud formation is described by a large-scale cloud scheme (Sundqvist et al. 1989). In the large-scale scheme, cloud droplet growth begins when the relative humidity exceeds a critical value (Stevens et al. 2013). Condensates are also produced by a mass-flux convection scheme (Tiedtke 1989; Giorgetta et al. 2013; Möbis and Stevens 2012) that parameterizes the mixing between updrafts and downdrafts with environmental air and transports heat, water vapor, and cloud condensate vertically through the column. The large-scale scheme includes the condensate detrained into the environment by the convection scheme as an additional source term (Giorgetta et al. 2013). Vertical turbulent mixing in ECHAM6 is described by a prognostic TKE scheme in which the production terms are wind shear and buoyancy (Giorgetta et al. 2013). The mixing strength is determined using K-theory coefficients that are functions of a turbulent mixing length, the static stability, and the TKE. To summarize, there are three separate schemes for large-scale evaporation/condensation, convection, and turbulent diffusion, each associated with their own moisture and temperature tendencies. Diabatic cooling by radiation must be balanced in equilibrium by some combination of these three processes. Our definition of radiative-convective equilibrium (RCE) requires that the temperature tendency from the convection scheme balance that from the radiative transfer scheme. RCE is satisfied in our simulations of the presentday climate (section 4a), but non-RCE states can also exist where moist convection contributes less to the atmospheric heat and moisture budget than the other two processes.

The mode of convection (i.e., shallow or deep) is determined by the strength of the large-scale moisture convergence (Möbis and Stevens 2012). In the column model, there is no large-scale, lateral transport, so only shallow convection occurs. Following P15, we specify an entrainment rate typical for deep convection of 0.1 km⁻¹ (Tiedtke 1989) in the shallow convection scheme to facilitate the formation of deep clouds without artificially specifying the surface convergence required for deep convection. This represents only a moderate change in the entrainment rate over the range for which ECHAM6 has been tested and tuned (Mauritsen et al. 2012).

4. Results

We perform simulations for the range of $0.01 \le \xi \le 1.85$. We use a handful of diagnostics to characterize the climate states: surface temperature; vertical cloud profiles; cloud radiative forcing (CRF), defined as the difference between the full-sky and inferred cloud-free radiative fluxes at the top of the atmosphere; and vertically integrated relative humidity (RH),

$$\langle \text{RH} \rangle = \frac{\int_{p_1}^{p_2} \text{RH } dp}{\int_{p_2}^{p_2} dp}, \tag{9}$$

where the angle brackets denote a pressure-weighted average and p_1 and p_2 are the pressure values at the boundaries of the atmospheric layer under consideration. The inferred cloud-free radiative fluxes used in determining the CRF at each model time step of the full-sky simulations are obtained, in practice, by making the clouds transparent in a separate radiation calculation.

Figure 1 shows the simulated cloudy climate states as ξ is varied. Climate states with similar patterns of cloud formation are classified as a group. These groupings are G1, G2, and G3 and correspond, respectively, to $0.01 \le \xi \le 0.14$, $0.16 \le \xi \le 1.63$, and $1.65 \le \xi \le 1.85$. Our description of G3 will be brief, as it is the subject of a companion work. The terms "low clouds" and "high clouds" pertain only to Earthlike states with two-layer clouds (i.e., G2).

a. The G2 climate

G2 extends through most of our parameter space, representing a continuum of vapor-poor and vapor-rich states with two-layer clouds (Figs. 1a,b) that have a negative net CRF (Fig. 2) and therefore cool the surface relative to a cloud-free atmosphere. G2 states are the most Earthlike and indeed most G2 states ($0.5 \le \xi \le 1.63$) are in RCE (Fig. 3a). The G2 low clouds are similar to cumulus clouds on the basis that their cloud fraction is ~20% (Fig. 3c) and the longwave flux divergence (LFD) at their cloud tops is typically several tens of watts per square meter less than the surface latent heat flux (LHF) (Figs. 4a,b), suggesting that these low clouds are generally maintained by turbulence from surface heating rather than cloud-top cooling (Fig. 5).

Across G2, the column water vapor increases from 0.2 to 2 cm (Fig. 6a). Remarkably, the column relative humidity

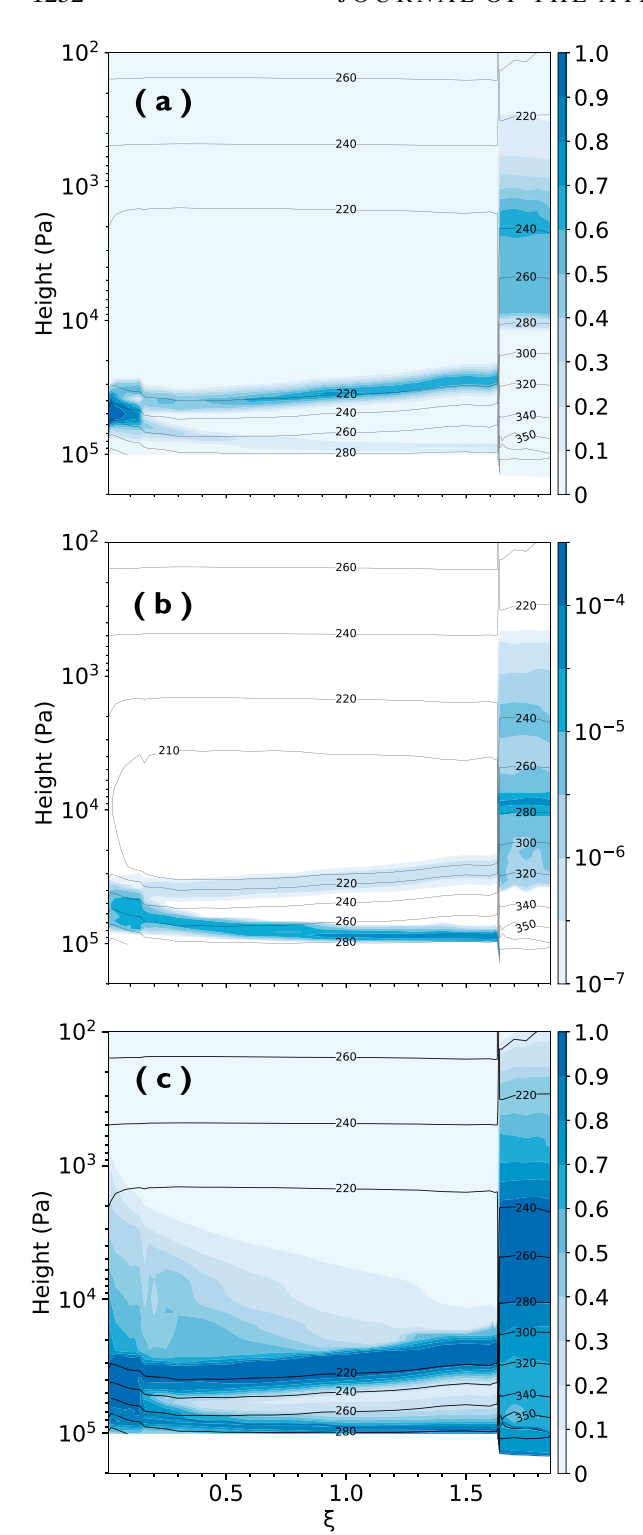


FIG. 1. Vertical profiles of (a) fractional cloud cover, (b) cloud condensate density (in kg m $^{-3}$), and (c) relative humidity. All variables are given as an average over the last 5 years of the simulation (the preceding statement applies to all figures in the paper, unless otherwise specified). Vertical axis is total pressure. Black contours denote temperature.

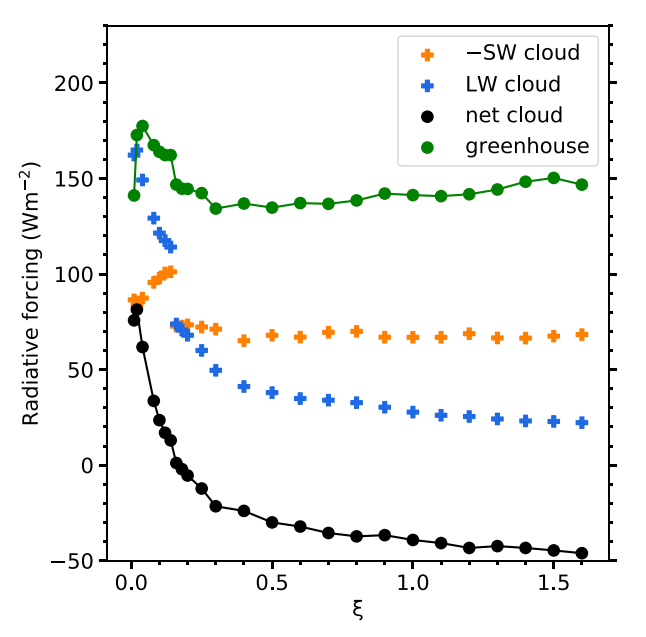


FIG. 2. Longwave (LW), shortwave (SW), and net cloud radiative forcing (CRF). The CRF is calculated as the difference between the cloudy and inferred clear-sky radiative fluxes at the top of the atmosphere. The clear-sky greenhouse forcing is calculated as the difference between the inferred clear-sky OLR and the surface emission.

($\langle RH \rangle = 65\%$), the albedo ($\alpha = 0.31$), and the surface temperature ($T_s = 290 \text{ K}$) are mostly invariant as ξ increases over the subset of G2 states in RCE (Figs. 3a, 6, and 7). One naturally wonders whether the tendency of RCE states to maintain fixed $\langle RH \rangle$, α , and T_s as moisture increases is because ECHAM6 is tuned to reproduce Earth's modern-day climate. If this behavior is observed in simulations with another climate model, it would point to robustness. We leave this to future work. For now, we offer a brief explanation for each invariant property of the G2 climate. First, the boundary layer is more humid than the free troposphere (Fig. 7), and this vertical contrast in relative humidity becomes more pronounced with increasing ξ . Based on Fig. 7, a consistent interpretation of the constant $\langle RH \rangle$ in G2 is the cancellation of a deeper and drier free troposphere and a thinner, wetter boundary layer. Second, α is constant because the SW cloud forcing is constant (Fig. 2), which can be traced back to relatively small variations in column cloud water and low cloud peak fraction (Figs. 3c and 6c). Third, over the range of ξ where T_s is roughly invariant, the magnitude of the change in the clear-sky greenhouse forcing and the net CRF are equal (\sim 15 W m⁻²) and opposite (Fig. 2), and thus cancel out. G2 clouds cool more with increasing ξ because the high clouds warm less (Fig. 2). Figure 3b shows that high clouds warm less because the clear-sky emission temperature drops, presumably from an increase in the infrared opacity of the atmosphere below the high clouds.

Not all properties of G2 climate are invariant, however. We find that the lapse rate decreases following the moist adiabat up from the lifting condensation level (Fig. 8), low clouds get lower and high clouds get higher (Figs. 1a,b), and the height

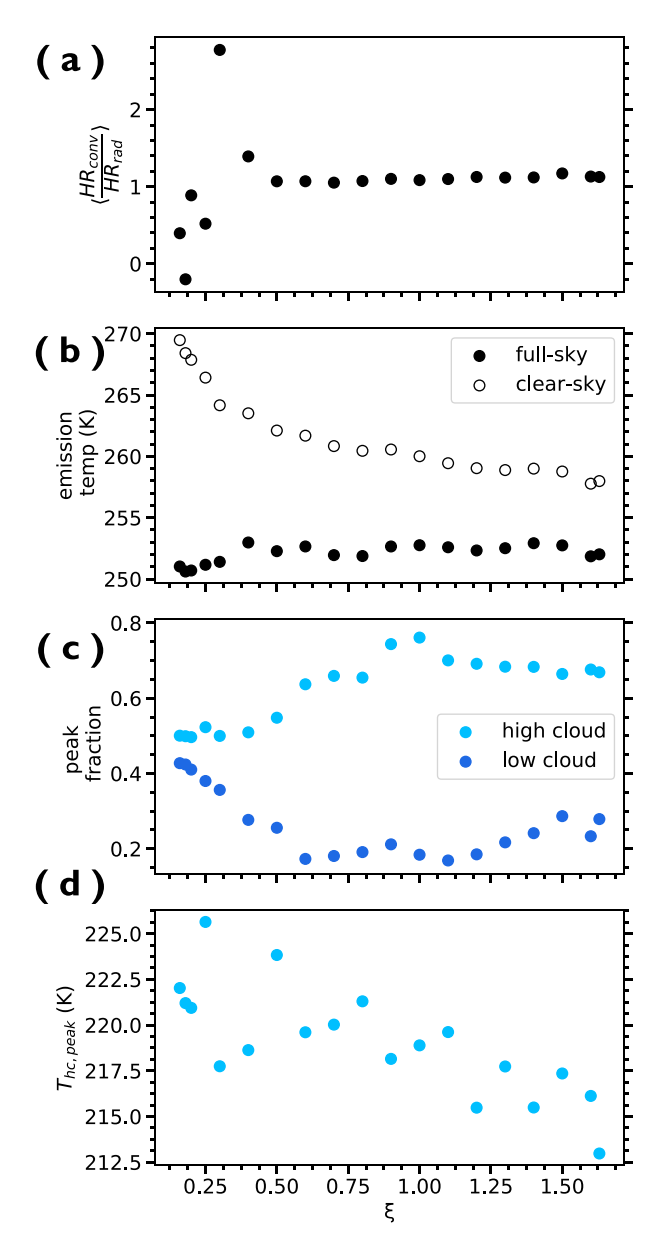


FIG. 3. (a) Pressure-weighted average of the ratio of the convective heating rate (HR_{conv}) to the radiative heating rate (HR_{rad}) (both in units of K day⁻¹) taken over the free troposphere. HR_{conv} is the temperature tendency from the convection scheme. By definition, RCE states possess a value of 1. (b) Full-sky and clear-sky emission temperature. The latter is inferred from the full-sky simulations in which clouds are made transparent in a separate radiation calculation. (c) Peak fraction of high and low clouds. (d) Temperature at the peak high cloud fraction, $T_{hc,peak}$.

of the boundary layer decreases between $\xi = 0.16$ and 1.0 but levels out between $\xi = 1.0$ and 1.63 (Fig. 9a).

Water vapor, and its RH in particular, governs the presence of two-layered clouds in the G2 states. In a convecting column, the RH has a "C-shaped" profile with local maxima at the outflow level and near the surface and low RH between. The midtropospheric RH minimum in Earth's tropics is a

consequence of environmental subsidence that balances outflow of detraining plumes at their equilibrium level, which is in competition with detrainment of moist plumes in the middle troposphere (Romps 2014). Note that this process is captured in entraining/detraining plume models of convection, in which case the relevant physics of upwelling plumes and environmental air is modeled in a single column, albeit as a parameterization (e.g., Tiedtke 1989). As a test of convection-controlled, C-shaped RH profile, we performed full-sky simulations with convection turned off, such that moisture is only affected by turbulent diffusion and condensation. This mechanism-denial experiment clearly lacks the midtropospheric RH minimum that is characteristic of the C-shaped profile (Fig. 10). Clouds are present in these full-sky simulations, but they no longer have distinct layers. We thus confirm that drying of the midtroposphere requires convection to induce environmental subsidence,² as analytically shown by Romps (2014).

b. Evaluating hypothesis 1: How high clouds get higher

In section 2a, we predicted that increasing ξ should cause high clouds to rise and cool. We also predicted from a theory of radiative transfer that the vapor pressure path (VPP) where high clouds form and longwave cooling rates decrease would take on a characteristic value of 1.2×10^4 Pa Pa_{ν}. Here, we evaluate those predictions, focusing on the location of the cloud maximum ("cloud level").

Most G2 states (0.5 $\leq \xi \leq$ 1.63) are in RCE (Fig. 3a), and in RCE one generally expects the physics of FAT to hold (Hartmann and Larson 2002). We thus restrict our analysis to the subset of G2 states in RCE. Figure 8 demonstrates that the lapse rate decreases as expected, relaxing toward the decreasing moist adiabatic lapse rate with increasing ξ . Figure 3d shows that the high cloud temperature decreases by 11 K. Is this quantitatively consistent with our ξ -modified FAT hypothesis? A crude estimate for the change in cloud temperature is obtained from a Taylor expansion of the Clausius–Clapeyron relation as

$$\Delta T \approx (\xi - 1) \frac{R_v}{L_{\rm hc}} T_{{\rm hc}, \xi=1}^2,$$
 (10)

where R_v is the specific gas constant of water, $T_{\text{hc},\xi=1}=219~\text{K}$ is the cloud temperature at $\xi=1$, and L_{hc} is the enthalpy of vaporization at 200 hPa. Evaluating Eq. (10) from $\xi=0.5$ to 1.63, a combined ΔT of $\approx-11~\text{K}$ would fix the SVP at cloud level. This estimate matches the actual temperature change in Fig. 3d. A reasonable conclusion is that the decrease in cloud temperature required by the physics of FAT coordinates with a decrease in the lapse rate to produce an upward shift of the high cloud, as observed in Fig. 11a.

The upward shift of the high cloud is consistent with the connection between clear-sky longwave cooling and high cloud formation (JF20b). In Fig. 11a, the cloud maximum is

² In a higher dimensional model like a GCM, large-scale downwelling and/or horizontal advection of air masses could also produce local minima in the vertical profile of RH.

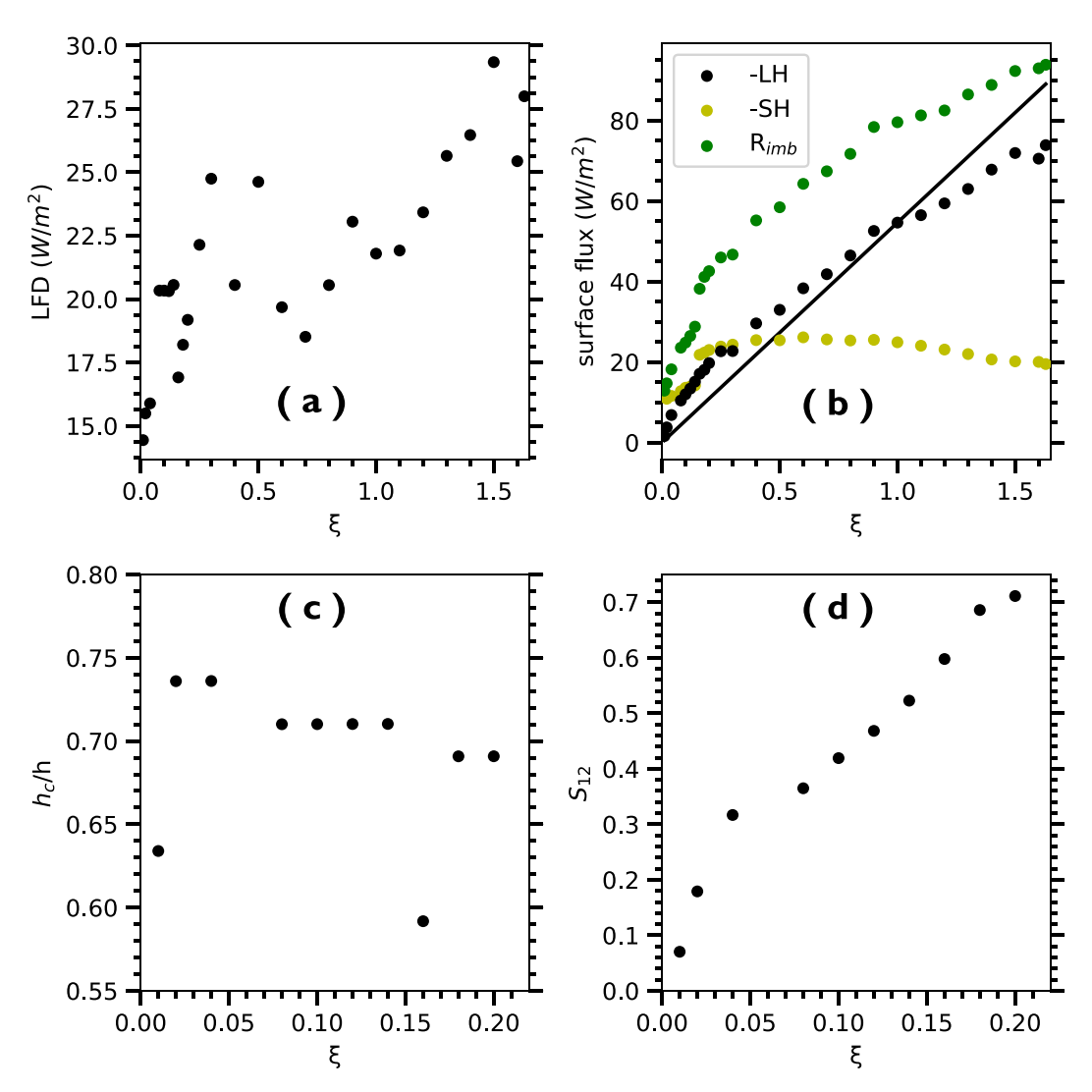


FIG. 4. (a) Longwave flux divergence (LFD) at the cloud top, (b) surface latent heat flux (black), sensible heat flux (yellow), and net radiative imbalance (green), (c) ratio of cloud thickness h_c to cloud-top height h, and (d) Sc instability parameter S_{12} . Note the x axis is different in each row. In (a), the values in G2 are from the *low* cloud top. The line in (b) is $y = \xi LHF(\xi = 1)$. Figure adapted from S19.

located in between a midtropospheric region where the clear-sky longwave cooling rate is relatively uniform and an upper-tropospheric region where the cooling rate drops toward zero. In general, increasing ξ causes the cooling rate above the lower troposphere to increase at each height (Fig. 11a). Figure 11b shows that the VPP between the top of the atmosphere and cloud level is $\approx 10^4$ Pa Pa_v in the RCE G2 states. The VPP varies by many orders of magnitude between the radiative tropopause ($\sim 10^3$) and the surface ($\sim 10^6-10^7$), so it is noteworthy that the upper-tropospheric decrease in longwave cooling occurs so close to its theoretically predicted value. The link between decreases in radiative cooling and cloud height in RCE is therefore supported by the data in Fig. 11.

Our observation of a roughly uniform VPP between the top of the atmosphere and cloud level in experiments that vary the SVP is perhaps the clearest demonstration to date in a numerical model of the key result of JF20b that the spectral properties of water vapor control the decrease in radiative cooling and thereby the cloud height. It would be desirable to test these ideas further in CRM simulations where the relevant physics are treated with greater fidelity than our 1D climate model.

c. Evaluating hypothesis 2: How the height of the cloud-topped boundary layer decreases

In section 2b, we hypothesized that low clouds get lower because the height of the cloud-topped CBL decreases as the tropospheric stability increases with increasing ξ . Here, we test that hypothesis.

Figure 5 shows that turbulent diffusion mixes heat and moisture in the G2 boundary layers and couples the low clouds to the surface. There are two fundamental sources of turbulence in any boundary layer: buoyancy and wind shear.

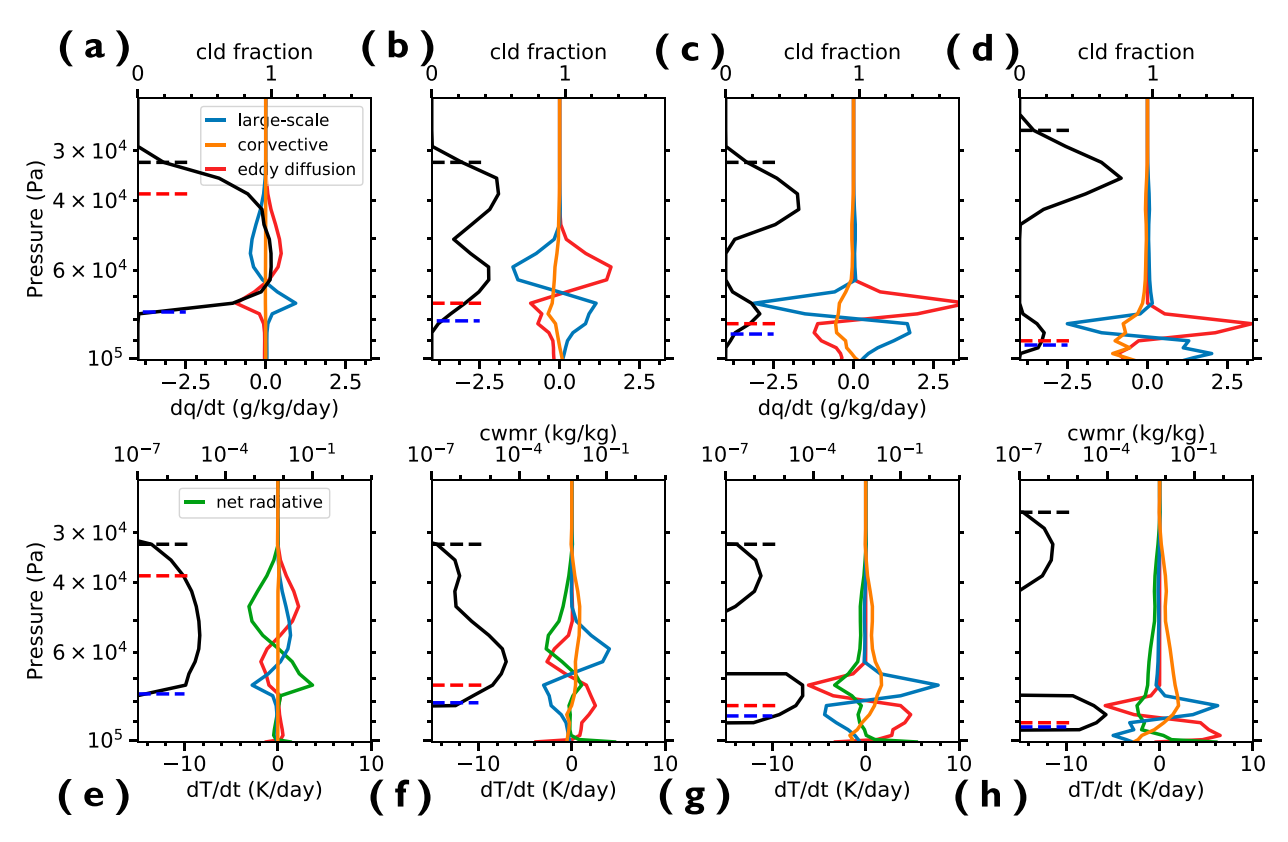


FIG. 5. (top) Moisture tendencies (color) and cloud fraction (black). (bottom) Temperature tendencies (color) and cloud water mixing ratio (cwmr; black). Profiles correspond to (a),(e) $\xi = 0.01$, (b),(f) $\xi = 0.16$, (c),(g) $\xi = 0.5$, and (d),(h) $\xi = 1.0$. Horizontal dashed lines on the left margins of each panel correspond to heights of the radiative tropopause (black), boundary layer (red), and lifting condensation level (blue).

Note that the vertical wind shear in the single-column model is predetermined and does not vary between experiments. The boundary layer height in ECHAM6 (h_{bl}) is set to be the largest of the CBL and the neutral boundary layer (NBL), $h_{bl} = \max(h_{cbl}, h_{nbl})$ (Stevens et al. 2013). The NBL is synonymous with the Ekman layer, which is always present on a rotating planet and where frictional dissipation of winds at the surface combines with Coriolis acceleration to aid in vertical mixing (Stull 1988). By estimating the depth of each boundary layer type, h_{cbl} and h_{nbl} , and comparing it to h_{bl} , we will show why h_{bl} drops when $\xi < 1$ and levels out when $\xi > 1$ (Fig. 9a).

The term h_{nbl} is the height where the effect of surface friction on the flow becomes negligible, which we estimate (Stevens et al. 2013; Stull 1988; Arya 1988):

$$h_{\rm nbl} = 0.3 \frac{u^*}{f}.$$
 (11)

This height primarily depends on the friction velocity $u^* = \sqrt{C_D}U$, where U is the prescribed wind speed above the surface and C_D is a momentum transfer coefficient, and the Coriolis parameter f. In Fig. 9a, we show $h_{\rm nbl}$ evaluated with a typical roughness length for a calm ocean surface of 1 mm, a wind speed of 6 m s⁻¹ at a height of 10 m, and the Coriolis parameter corresponding to Earth's rotation rate at a latitude of 38°N. Both $h_{\rm nbl}$ and $h_{\rm bl}$ are approximately fixed

at a height of 1 km when $\xi \ge 1$ (Fig. 9a), indicating that shear- rather than buoyancy-driven turbulence is deeper in the vapor-rich G2 states.

The term $h_{\rm cbl}$ represents the maximum height reached by positively buoyant eddies rising from the surface [Eq. (8)]. Estimating $h_{\rm cbl}$ requires information about the bulk thermodynamic state of the boundary layer and free troposphere in G2. Pressure-weighted averages are carried out over two atmospheric slabs corresponding to 1000–700 and 700–400 hPa when $\xi < 0.9$ and 1000–850 and 850–400 hPa when $\xi \ge 0.9$, which is found to give the best agreement between $h_{\rm cbl}$ and $h_{\rm bl}$. Both are plotted in Fig. 9a. To understand why $h_{\rm cbl}$ decreases over G2, we normalize each term on the rhs of Eq. (8) by their reference value at $\xi = 1$. The nondimensionalized terms are

(i)
$$\Theta_{v}|_{s}/\Theta_{v}|_{s}(\xi=1)$$
,

(ii)
$$[\overline{w'\Theta'_{\nu}}|_{s}/\overline{w'\Theta'_{\nu}}|_{s}(\xi=1)]^{2}$$
,

(iii)
$$\left[\Delta\Theta_{v}/\Delta\Theta_{v}(\xi=1)\right]^{-3}$$
,

(iv)
$$[a_c/a_c(\xi=1)]^{-3}$$
.

Terms (i)–(iv) are plotted in Fig. 13a, revealing that a partial cancellation between (iii) and (iv) mostly explains the change

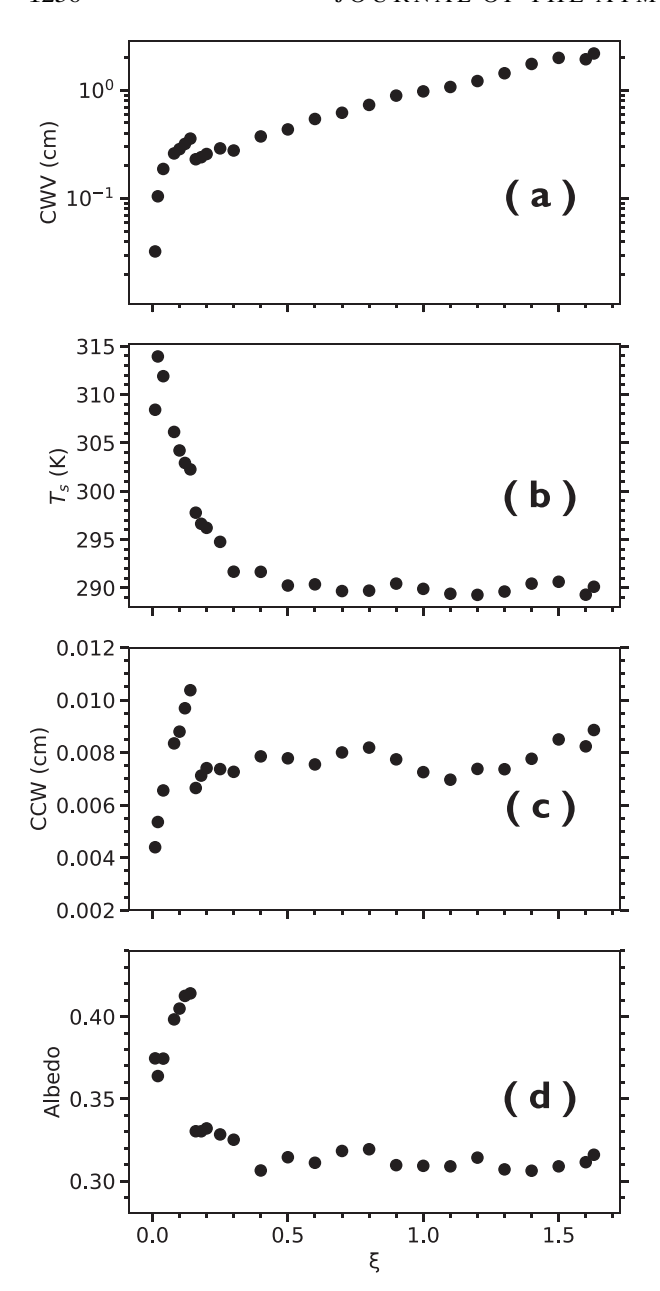


FIG. 6. (a) Column water vapor (CWV), (b) surface temperature T_s , (c) column cloud water (CCW), and (d) albedo. Albedo is computed as the ratio of upwelling shortwave over downwelling shortwave at the top of the atmosphere.

in h_{cbl} . The decrease in (iii) is facilitated by the decrease in the lapse rate (Fig. 8), which causes the potential temperature in the free troposphere to increase more rapidly than in the boundary layer (Figs. 12 and 13b). The increase in (iv) can be understood from Eq. (12), which is an empirical fit to LES experiments of cloud-topped mixed layers (Cuijpers and Duynkerke 1993):

$$a_c = 0.5 + 0.36 \tan^{-1}(1.55\,\tilde{Q}).$$
 (12)

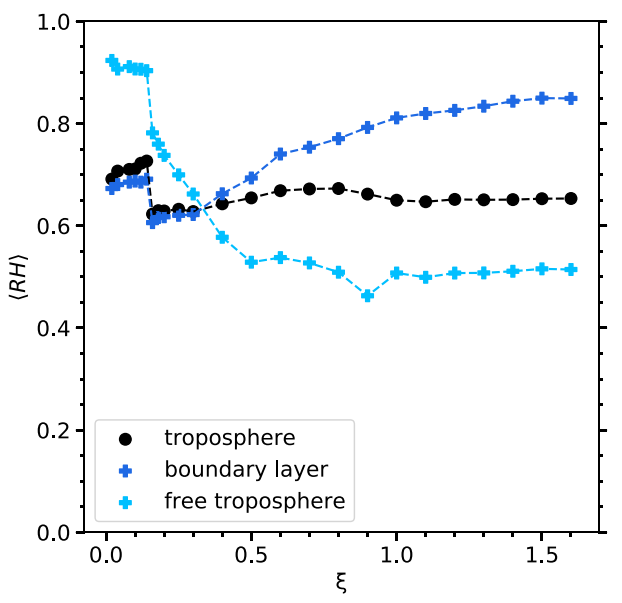


FIG. 7. Column-integrated relative humidity $\langle RH \rangle$ of the troposphere (black), boundary layer (dark blue), and free troposphere (light blue). Variables calculated using Eq. (9).

Equation (12) diagnoses the (moist) convective area fraction as a function of a single parameter, the normalized saturation deficit (Cuijpers and Bechtold 1995),

$$\tilde{Q} = \frac{dq^{\rm BL}}{\sigma_a^h},\tag{13}$$

where $dq^{\rm BL}=q^{\rm BL}-q^{\rm BL}_{\rm sat}$ is the boundary layer saturation deficit and σ_q^h [Eq. (14)] is the square root of the moisture variance at the top of the boundary layer. \tilde{Q} is a statistical measure of the potential for turbulent moisture fluctuations at the top of the boundary layer to meet the requirements for latent heat release. More negative values of \tilde{Q} indicate that moisture fluctuations σ_q^h are less likely to overcome the boundary layer saturation deficit. We evaluate Eq. (13) over G2 and find that increasing ξ causes \tilde{Q} to become more negative. To understand why, we normalize each term in Eq. (13) by their value at $\xi=1$, and plot the result in Fig. 13c. The moisture variance at the top of the boundary layer (N06; Neggers et al. 2007),

$$(\sigma_q^h)^2 = \overline{w'q'} \frac{\Delta q}{\Delta z} \tau, \tag{14}$$

is the product of three parts: the absolute moisture gradient across it $(\Delta q \text{ increases as } \xi \text{ increases})$, the eddy moisture flux from the surface $(\overline{w'q'})$ increases as ξ increases), and the large-eddy turnover time scale $(\tau = h_{\text{cbl}}/w^*)$ decreases as ξ increases) (Fig. 13d). Ultimately, increasing ξ amplifies σ_q^h (Fig. 13c). However, this amplification of σ_q^h is insufficient to close the widening saturation deficit dq^{BL} . Why does increasing ξ widen the saturation deficit (Fig. 13c)? Consider a perturbation scenario where ξ is increased in a parcel of BL air initially at

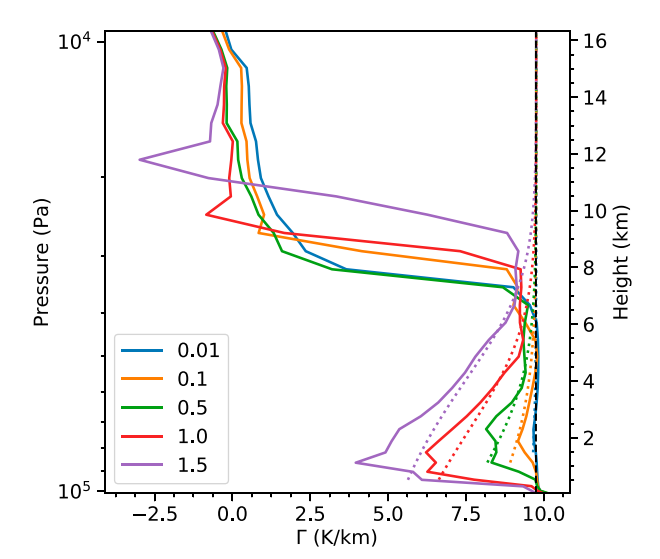


FIG. 8. Lapse rate (Γ) as a function of height for a range of ξ . Dotted lines give the respective moist adiabatic lapse rate from the lifting condensation level (Romps 2017). For reference, the dry adiabatic lapse rate is plotted as a dashed black line.

 $\xi=1$ while its RH and temperature are conserved. The specific humidity of the parcel must increase and after the perturbation is given by $q=\xi q^*$ where $q^*=\mathrm{RH}q^*_\mathrm{sat}$. The parcel's "distance" from saturation is increased from $dq^*=q^*-q^*_\mathrm{sat}$ (before the perturbation) to $dq=q-q_\mathrm{sat}=\xi dq^*$ (after the perturbation). If this scenario applied, on the whole, to the boundary layer in our experiments, $dq^\mathrm{BL}/dq^\mathrm{BL}(\xi=1)$ would vary linearly with ξ . This is found roughly to be the case in Fig. 13c, even though the requirements (that would align the experiments with this hypothetical scenario) of fixed RH and temperature do not strictly hold. Therefore, \tilde{Q} becomes more

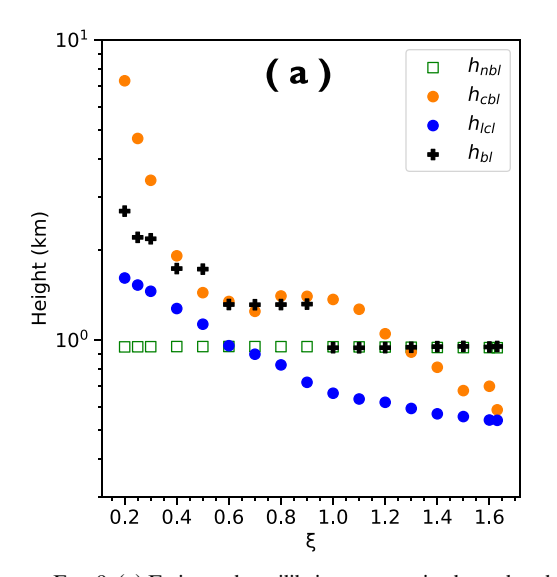
negative as SVP increases (Fig. 13c) because the saturation deficit grows faster than the moisture fluctuations at the top of the boundary layer, fewer rising thermals meet the requirements for latent heat release, and term (iv) increases (Fig. 13a).

Summarizing this result, the decrease in $h_{\rm cbl}$ is driven by the dependence of the thermodynamic variables, T and q, on ξ . T depends on ξ because moist convection mixes along the moist adiabat, so increasing moisture reduces the vertical gradient in temperature and term (iii) in turn. Term (iv) increases because the mean-state saturation deficit increases faster than the moisture fluctuations at the top of the boundary layer. Terms (iii) and (iv) have opposite effects on the height of the CBL, so an increase in tropospheric stability ultimately drives the decrease in $h_{\rm cbl}$.

Assembling all the pieces, we have a consistent story for why low clouds get lower. Low clouds get lower because they are coupled to the height of the CBL. Increases in tropospheric static stability $(\Delta\Theta_v)$ are the primary driver of the decrease in $h_{\rm cbl}$ (as ξ increases, the vertical length scale of buoyancy-driven turbulence decreases). An important correction to hypothesis 2 is that low clouds get lower only when the deepest mixing occurs through buoyancy- rather than shear-driven turbulence as ξ increases. Indeed, low clouds level out when $h_{\rm nbl} > h_{\rm cbl}$.

d. The G1 climate

G1 is a vapor-poor, warm, and humid regime with single-layer clouds that stretch from 800 to 300 hPa. The phenomenology of the G1 cloud supports an analogy to unbroken Sc clouds under an inversion. Peak cloud fraction decreases from 100% to 80% over G1 (e.g., Fig. 1a), values that are 20%–40% greater than the extensive Sc that form off the western coast of Earth's continents (Wood 2012) but comparable to the coverage observed in limited-domain CRM simulations of Sc (Tan et al. 2017; S19)



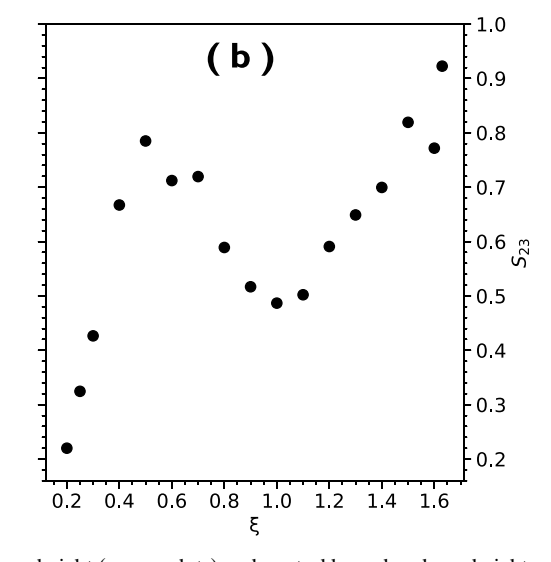


FIG. 9. (a) Estimated equilibrium convective boundary layer height (orange dots) and neutral boundary layer height (square). Plus signs (+) mark the actual boundary layer height. The height of the lifting condensation level (blue dots) is determined analytically (Romps 2017). (b) Low cloud instability parameter S_{23} , calculated from the data in (a) with Eq. (16).

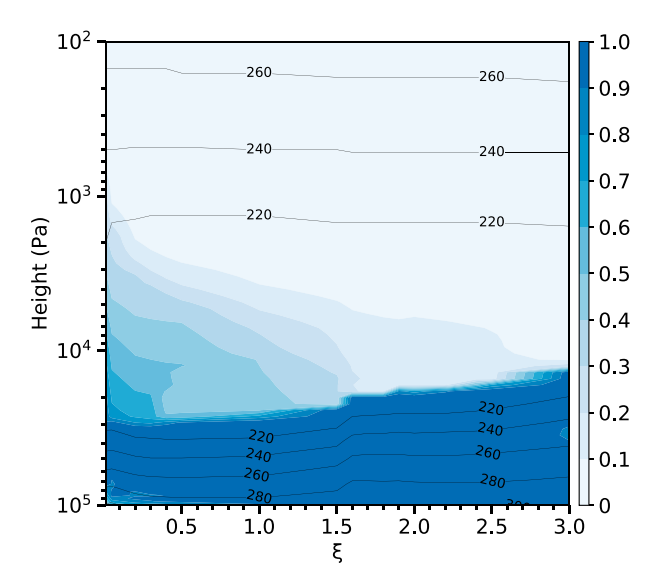


FIG. 10. Vertical profile of relative humidity in full-sky simulations where convection is disabled. Vertical axis is total pressure. Black contours denote temperature.

over SSTs of 290 K. The LFD at the cloud top (in units of W m⁻²) is larger than surface LHFs (Figs. 4a,b), resembling an Sc-like regime where buoyancy fluxes at the cloud top rather than at the surface are most important to the production of boundary layer turbulence. Unlike Sc on Earth, the G1 cloud spans most of the troposphere so that the cloud top rests under

a resolved (stratospheric) temperature inversion. In addition, the G1 cloud warms, rather than cools, the climate, producing surface temperatures as high as 315 K (Fig. 6b). How is this possible? The free troposphere has higher RH than the boundary layer in this regime (Fig. 7), and this produces a thick, quasipermanent cloud that cools to space in the upper troposphere (Fig. 5e). As ξ decreases, the environmental lapse rate converges on the dry adiabatic lapse rate, thus maximizing the temperature contrast across the cloud. With these factors combined, the G1 cloud generates a LW CRF that greatly exceeds its SW CRF. This is somewhat surprising because G1 states have about a 30% higher albedo than G2 states (Fig. 6d). The fact that both G1 and G2 have similar amounts of column-integrated cloud water (Fig. 6c) but the G2 low cloud fraction is up to 75% lower (Figs. 5 and 3c) likely explains the overall difference in albedo.

In Figs. 5a and 5e, we show the cloud fraction, cloud water mixing ratio, and temperature and moisture tendencies for the end-member G1 state, $\xi=0.01$. Interestingly, convection contributes little to the atmospheric heat and moisture budget relative to diffusive and large-scale processes. A consistent interpretation is as follows. Radiative cooling at the cloud top facilitates large-scale condensation that is communicated to lower layers through reevaporation, radiative heating balances the evaporative cooling, and boundary layer diffusion resupplies the precipitated moisture. Radiative cooling raises the upper-tropospheric RH, triggering cloud formation through large-scale condensation. Lower-tropospheric radiative heating is the result of a cloud greenhouse effect and keeps the air there subsaturated.

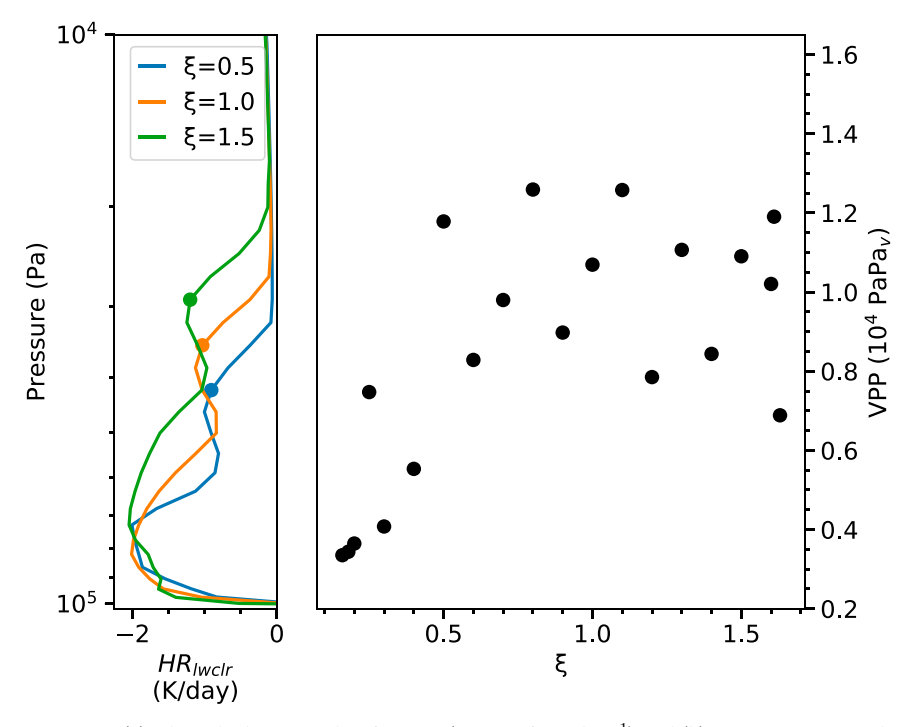


FIG. 11. (a) Clear-sky longwave heating rate (HR_{lwclr} ; in K day⁻¹) and (b) vapor pressure path (VPP; in Pa Pa_v) between the top of the atmosphere and cloud level for a range of ξ . The heating rates at cloud level are marked by dots in (a).

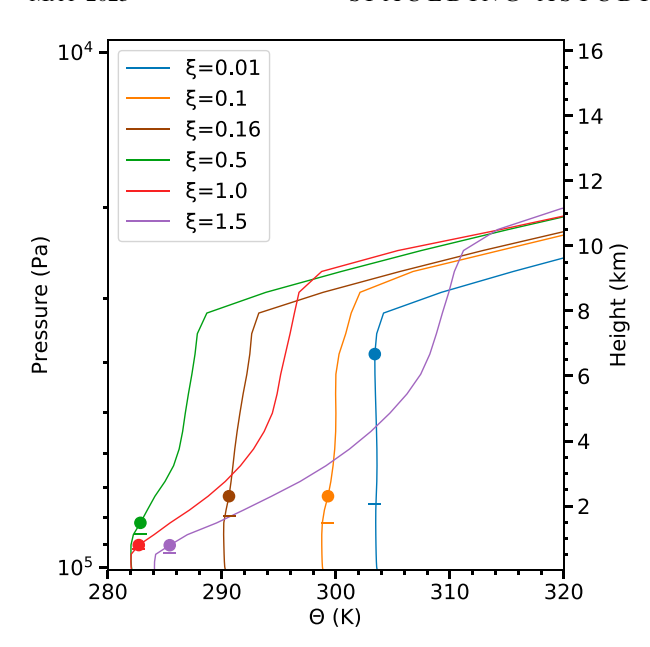


FIG. 12. Vertical profile of potential temperature (solid lines), boundary layer height (circles), and lifting condensation level (horizontal ticks) for a range of ξ .

e. Evaluating hypothesis 3: How single-layer G1 clouds break up

In section 2c, we hypothesized that there exist vapor-poor states where there is no vertical separation between cloud layers. This hypothesis emerges intuitively from the prediction that low clouds get higher and high clouds get lower as the moisture content of the atmosphere is reduced. Here, we test that hypothesis through analysis of the simulations and show that the transition from single-layer to two-layer clouds can be interpreted through a cloud instability parameter.

Figures 5 and 14 tell most of the story. To aid our description, we define two distinct mixing layers. The "diffusive layer" and "convective layer" extend from the surface and the LCL, respectively, to the height where their respective moisture and temperature tendencies in Fig. 5 drop to zero. In G1, the diffusive and convective mixing layers overlap. As ξ increases, the shallowing diffusive layer separates from the convective layer which continues to top out at the radiative tropopause (Figs. 5f-h). An important consequence of this separation is that control over the heat and moisture budget of the upper troposphere shifts to moist convection. The competition between convective detrainment and environmental subsidence in this region produces an RH minimum that first emerges around 400 hPa at $\xi = 0.14$ and then descends (Fig. 14), tracking the separation level. When the upper troposphere becomes decoupled from surface turbulence, moist convection maintains a thin high cloud by transporting condensed water into this region.

In sections 4c and 4a, we extended an analogy between G1 clouds, G2 low clouds, and two different types of boundary layer clouds on Earth, Sc and Cu, respectively. Is G1 to G2 an Sc to Cu transition? To determine whether this is the case, we

evaluate an Sc instability parameter, here denoted S_{12} , adapted from Bretherton and Wyant (1997, henceforth BW97) that represents the minimum requirements for the decoupling of an Sc cloud from the surface:

$$S_{12} = \frac{\text{LHF}}{\text{LFD}} \frac{h_c}{h},\tag{15}$$

where h_c is the cloud thickness and h is the height of the cloud top. Entrainment (a process that mixes dry air downward and moist air upward) dries the cloud layer in an absolute sense. Radiative cooling at the top of Sc clouds causes air to be negatively buoyant, driving a turbulent circulation within the boundary layer that resupplies moisture to the cloud. In BW97's minimal model of a nonprecipitating Sc deck, entrainment warming and radiative cooling balances the energy budget while entrainment drying and convective moistening (proportional to the surface LHF) balances the moisture budget.

BW97 predict that Sc clouds risk decoupling from the surface and breaking up when $S_{12} > 0.55$, and this was reproduced in LES simulations by S19. To calculate the LFD in W m⁻² (Fig. 4a), we take the peak longwave heating rate in W m⁻³ at the cloud top and then multiply this peak value by the average distance (500 m due to numerical resolution) between the cloud top and the next vertical level. Following \$19, we assume the cloud base is where the fractional cloudiness goes above 5%. S_{12} increases between $\xi = 0.01$ and 0.14 because the surface LHF increases fivefold (500% increase) from 3 to 15 W m⁻², the cloud-top LFD increases by 40% from 14 to 20 W m⁻², and h_c/h varies by 14% (Fig. 4). A theoretical prediction for the change in LHF with increasing ξ is given in Fig. 4d using the bulk-aerodynamic formula for LHF where RH and T at the surface are fixed. The theoretical prediction agrees reasonably well with the actual change in the LHF. Judging by Fig. 4d, the G1 cloud splits when $S_{12} \approx 0.55$ (or equivalently $0.14 < \xi < 0.16$). We conclude that the instability parameter predicts when the G1 cloud splits in our simulations, lending support to the idea that G1 to G2 is an Sc to Cu transition.

S19 increased CO₂ concentrations in LES simulations of Sc clouds, and found that all terms in Eq. (15) play a relatively important role in driving S_{12} sufficiently high that the cloud deck becomes unstable. In this study, we vary water vapor and find that the quasi-linear dependence of the surface LHF on ξ is by far the dominant factor destabilizing the G1 cloud. Interestingly, our result is qualitatively similar to BW97's LES experiments where, instead, increasing SSTs caused the surface LHF to increase by a factor of 5. We find a 50% reduction in maximum cloud fraction from 0.8 to 0.4 crossing from G1 and G2 (or a 75% reduction from 1.0 to 0.25 if comparing the driest G1 state to the low cloud in the wettest G2 state). The liquid water path decreases as the G1 cloud breaks up in our simulations (Fig. 6c), which we attribute to a reduction in cloud water content due to midtropospheric subsidence drying (Figs. 5e,f) and less efficient transport of moisture by convection relative to turbulent diffusion. Contrary to what one would expect from an Sc to Cu transition, the temperature

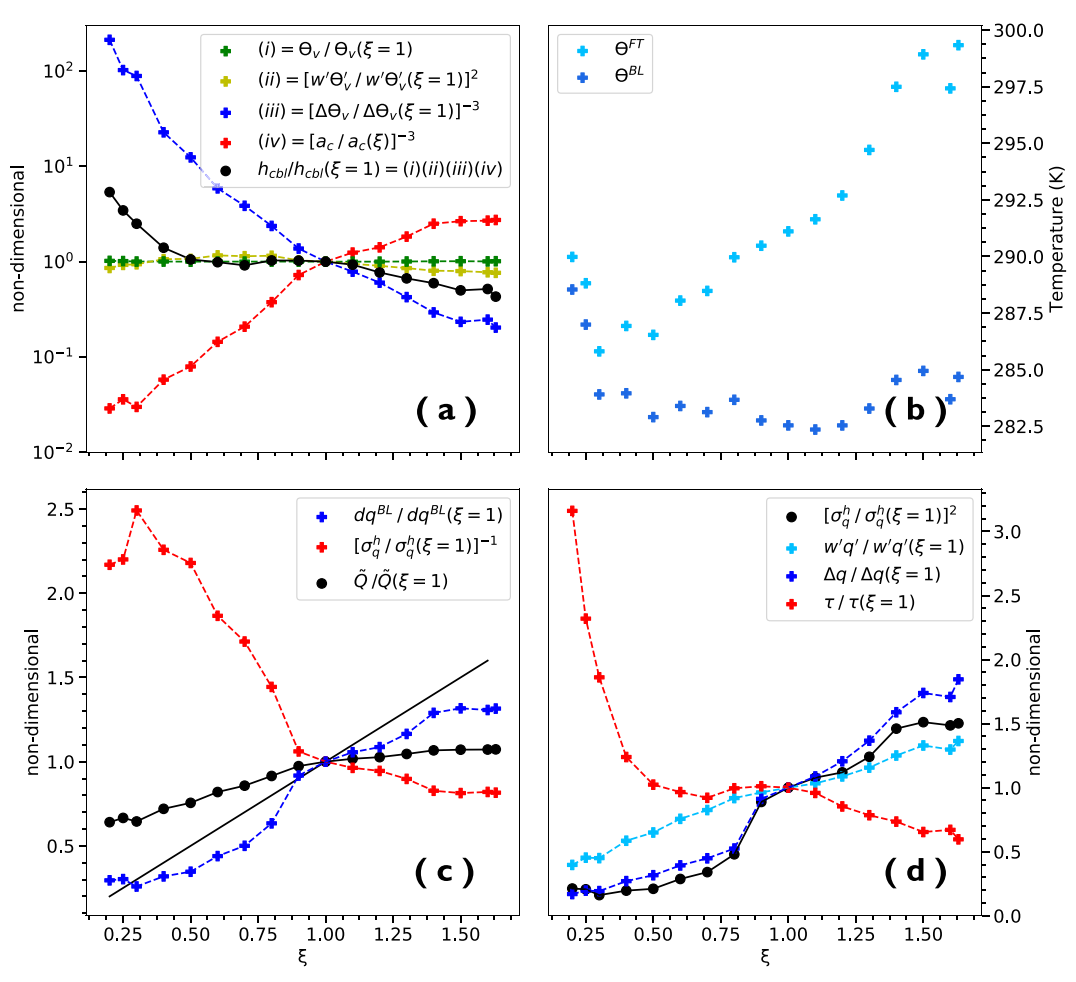


FIG. 13. (a) Key terms from Eq. (8) normalized by their value at $\xi = 1$. (b) Average potential temperature of the free troposphere $\Theta^{\rm FT}$ and boundary layer $\Theta^{\rm BL}$, respectively, from Eq. (6b). (c) Key terms from Eq. (12) normalized by their value at $\xi = 1$. The black line in (c) is $y = \xi$. (d) Key terms from Eq. (14) normalized by their value at $\xi = 1$. See the text for more details.

change across the transition is negative. The G1 cloud deck has a positive net CRF so that when it breaks up the cloud warming effect is *diminished* and the surface temperature *decreases*.

In summary, our simulations confirm hypothesis 3: that vapor-poor states have a single- rather than double-layer cloud structure. We conclude that the effect of increasing ξ is to reduce the influence of turbulent diffusion in the troposphere from the top down, handing off the role of cloud formation in this region to moist convection through its well-studied effect on the moisture budget (Romps 2014). As the diffusive mixing layer shallows with increasing ξ and separates from the convective mixing layer, moist convection produces an RH minimum at the separation level and maintains a thin high cloud at its top. The G1 cloud fractures when it meets the minimum requirements for an Sc deck to decouple from the surface (BW97). The breakup of this surface-warming cloud generates a sharp, 5 K drop in surface temperature (Fig. 6b). From these considerations, we argue that G1 to G2 is an atypical Sc-to-Cu transition.

f. The G3 climate

G3 is a hot, vapor-rich regime with a surface temperature of 360 K. In the annual mean, the G3 atmosphere has the characteristic structure of the moist greenhouse (P15; Wolf and Toon 2015) with a humid inversion layer near the surface, a subsaturated middle troposphere, and a cloudy upper troposphere (Fig. 1). The G3 states hold approximately 5 m of precipitable water in the atmospheric column (not shown), or over 100 times more water than at $\xi = 1$. This magnitude of atmospheric moisture makes the G3 states the most Titan-like (Tokano et al. 2006). We will explore connections between G3 and Titan's climate in a companion paper.

g. Evaluating hypothesis 4: How a cloud instability causes low G2 clouds to break up

Our simulations confirm hypothesis 4, that there exist vapor-rich states with elevated, single-layer clouds (Figs. 1a,b). This result is consistent with many previous studies, which report the partial to total destruction of low clouds when the

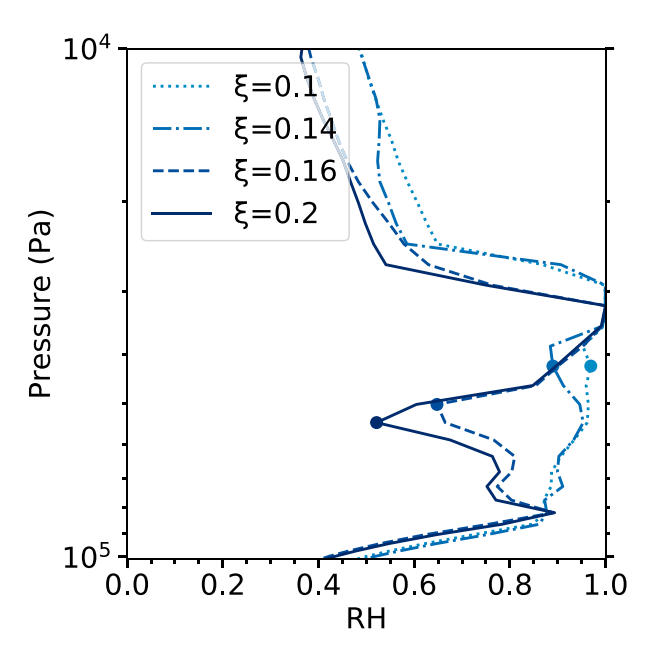


FIG. 14. Profiles of relative humidity across the G1-to-G2 transition for $\xi = 0.1$, 0.14, 0.16, and 0.2. Filled circles correspond to the location where the positive diffusive moisture tendency (as in Fig. 5) moving upward goes to zero.

concentration of greenhouse gases in the atmosphere rises beyond a threshold value (Leconte et al. 2013; P15; Wolf and Toon 2015; S19; Seeley and Wordsworth 2021). In the parameter space that we examine, low clouds disappear when $\xi \approx 1.65$. Low clouds are the largest source of planetary albedo in G2. Figures 15a and 15c show that their disappearance produces an energy imbalance at the top of the atmosphere. This energy imbalance generates warming and an influx of water vapor into an expanding troposphere. Enhanced concentrations of water vapor then close the infrared windows to space, which causes radiation to converge in the lower troposphere (Fig. 15b). It has been argued that an inability of the lower atmosphere to radiatively cool in vapor-rich atmospheres elevates the cloud profile (Leconte et al. 2013), and prevents low clouds from (re)forming. We also adopt this perspective. High clouds thicken and brighten, bringing the column back into energy balance (Figs. 15a,c).

Convergence of radiation into the lower troposphere likely explains the lack of low clouds in G3, but not why they disappear in the transition from G2. The solution is to examine another fundamental constraint on low cloud formation—one that has not been considered elsewhere. It is clear that moisture is resupplied to G2 low clouds by turbulent diffusion. The height reached by positively buoyant eddies in the boundary layer is given by $h_{\rm cbl}$ [Eq. (8)]. The height to which a surface parcel must be lifted in order to saturate is $h_{\rm lcl}$ (Romps 2017). Low clouds cannot form if the LCL comes to lie outside of the convective boundary layer, or in other words if boundary layer turbulence cannot lift moist parcels to the height where they condense. We quantify this effect with an instability parameter:

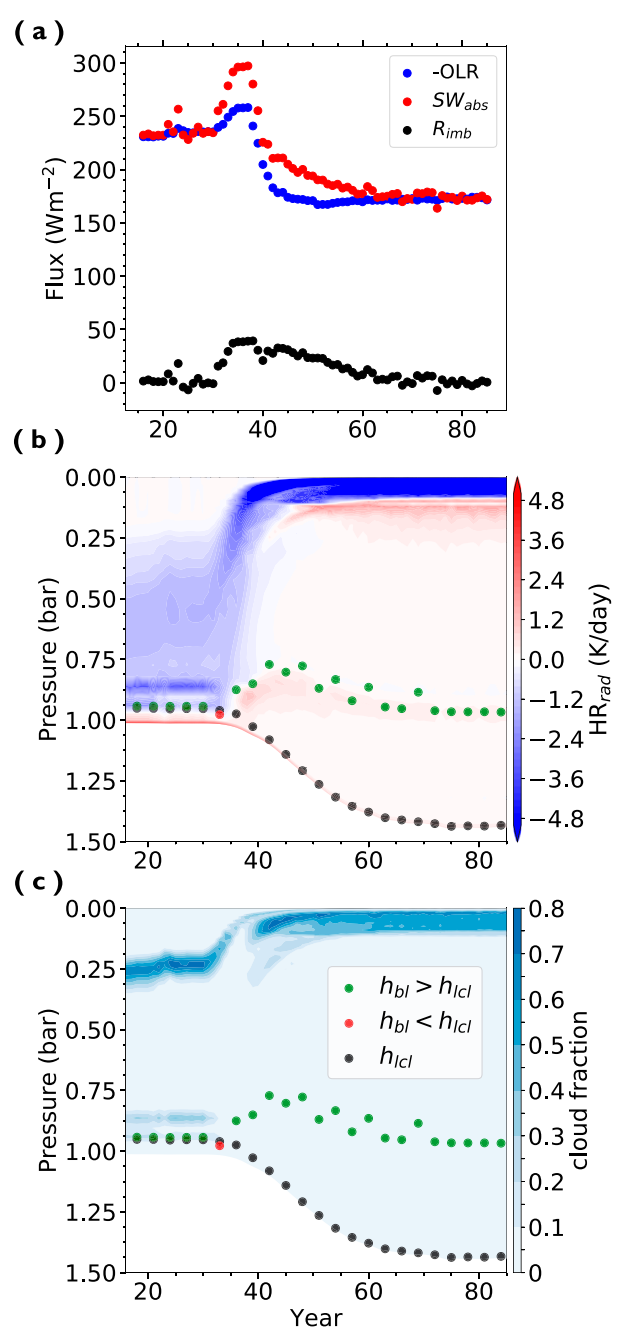


FIG. 15. Visualization of the G2-to-G3 transition for $\xi=1.65$. (a) Outgoing longwave radiation (OLR), absorbed shortwave radiation (SW_{abs}), and radiative flux imbalance ($R_{\rm imb}$) at the top of the atmosphere (in W m⁻²). Hovmöller diagrams of the (b) radiative heating rate (HR_{rad}, in K day⁻¹) and (c) fractional cloud cover with the height of the boundary layer ($h_{\rm bl}$) and the lifting condensation level ($h_{\rm lcl}$) overlain. The data are time averages over each year of the simulation. In (b) and (c), $h_{\rm bl}$ and $h_{\rm lcl}$ are given every third year to minimize overcrowding. The horizontal axis is the time in years since the start of the simulation. The vertical axis in (b) and (c) is total pressure and the legend for both panels is shown in (c). Low clouds disappear in year 33 of the simulation when $h_{\rm bl} < h_{\rm lcl}$.

$$S_{23} = \frac{h_{\rm lcl}}{h_{\rm cbl}}. (16)$$

If this parameter adequately describes when low clouds can form, then low clouds should break up when $S_{23} > 1$. We compute S_{23} using the values for $h_{\rm cbl}$ and $h_{\rm lcl}$ from Fig. 9a. Figure 9b confirms that low clouds disappear when S_{23} approaches 1. What causes the nonmonotonic trend in S_{23} ? First, $h_{\rm lcl}$ drops as ξ increases, presumably due to an increase in near-surface RH (Fig. 7) associated with the shallowing CBL (Rieck et al. 2012) and enhanced surface LHF (Fig. 4b). However, $h_{\rm cbl}$ decreases more rapidly than $h_{\rm lcl}$ for increasing $\xi < 0.5$ and $\xi > 1$ and less rapidly in between, and this is sufficient to explain the nonmonotonic behavior of S_{23} and thus the eventual destabilization of the low clouds.

Our simulations confirm that the breakup of low clouds triggers a climate transition into a state with elevated, single-layer clouds. We offer a constraint for low cloud formation S_{23} at the onset of this transition that combines only two basic ingredients, the depth of the CBL and the height of the LCL. We find that S_{23} is consistent with a low cloud breakup event at $\xi \approx 1.65$ where it crosses a critical value. Figure 15c confirms that low clouds disappear in the same year of our $\xi = 1.65$ simulation that the boundary layer drops below the LCL. This destabilizes the G2 low clouds by starving them of their supply of surface moisture.

5. Discussion

In our G2 simulations, the climate is insensitive to ξ over a wide range. A possible explanation for this is that ξ is varied by a single order of magnitude, whereas the SVP varies by many orders of magnitude over the depth of Earth's troposphere. The climate could be more sensitive to ξ as the change in temperature between the surface and the tropopause decreases (typical estimates for Earth and Titan differ by about a factor of 1/3). Titan's climate could also be less sensitive to ξ because the ratio L_{ν}/R_{ν} in the Clausius–Clapeyron relation for water at 290 K is greater than methane at 90 K by a factor of 5 (here neglected). These thermodynamic differences are likely to be important in any modeling effort to bridge the space between Earth's and Titan's respective climates.

Our numerical experiment varying ξ showed that the vapor pressure path at the high cloud level in RCE states is close to its theoretically predicted value and therefore in support of the theory of JF20b that the spectral properties of water vapor control the decrease in longwave cooling at the top of the troposphere. Our result that high clouds rise and cool is broadly consistent with the physics behind the FAT hypothesis and a previous study that artificially increased the radiative effect of water vapor in the upper troposphere of a CRM (Harrop and Hartmann 2012). By identifying a constant VPP across a broad range of ξ , our study provides strong support of the FAT hypothesis.

We tested fundamental concepts about cloud heights in atmospheres much different than our own by varying ξ . As demonstrated by JF20b, spectroscopic studies can offer deep

insight into cloud formation. We raise the possibility that cloud heights in any atmosphere in RCE with a dominant condensing absorber might be inferred from the unique distribution of its absorption coefficient. Future modeling studies could consider a Titan-like atmosphere with methane as the dominant absorber and radiatively infer the cloud height. The radiative cloud height could then be readily compared to observations of cloud heights on Titan.

The response of the G2 low clouds to increasing ξ is consistent with prior work. In the tropics, the vertical potential temperature gradient is known to increase as the climate warms because the lapse rate is close to moist adiabatic, Γ_m (Wood and Bretherton 2006). Bretherton et al. (2013) carried out two different sets of LES experiments of Sc- and Cu-topped boundary layers in which they increased the temperature of the free troposphere (FT) while keeping the surface temperature fixed (or warming it less than the FT). In both cases, they found a reduction in boundary layer entrainment and low cloud height. In our simulations, the CBL ultimately drops with increasing ξ because the FT warms faster than the boundary layer (because of invariant surface temperatures in G2 states) as Γ_m decreases (Fig. 13b). This is qualitatively similar to the outcome of "inversion strength" experiments detailed in Bretherton et al. (2013).

The CBL framework of N06 assumes that the cloud-top buoyancy fluxes that induce entrainment are proportional to the surface fluxes [see Eq. (4)] and, therefore, is of limited use outside Cu-like regimes where cloud-top radiative cooling is of greater importance. The inability to account for changes in cloud-top buoyancy fluxes associated with radiation is a limitation of the N06 framework (note that this framework is interpretative and is not part of ECHAM6). Figure 4a shows that longwave cooling at the top of the low clouds generally increases with increasing moisture, and this should promote boundary layer entrainment. The diagnosed decrease in CBL height suggests that radiative changes at the cloud top are, at best, of secondary importance to stability changes in our simulations. The N06 estimate for CBL height is only diagnostic, and therefore, it would be desirable to test this behavior in a CRM.

The simulations presented in this study could be interpreted as representing a range of cloud regimes over pole-to-equator conditions on Earth. For context, consider the change in surface temperature that represents the surface vapor pressure change over $0.01 \le \xi \le 1.85$. Adapting Eq. (10) to the surface environment, one finds that this range of ξ corresponds to a 32 K change in temperature, from 273 to 305 K. We extended an analogy in this study between G1 clouds and Sc as well as G2 low clouds and Cu. In nature, these cloud types are correlated with different SSTs (Cesana et al. 2019). Interestingly, the transition from G2 low clouds to G1 clouds occurs at low ξ , which may correspond to cooler and drier conditions on Earth.

Our simulations may be analogous to Earth's past, present, and future climates, of which we offer two examples. First, CRM simulations initiated at 305 K with a solar constant 10% higher than the modern day are climatologically unstable and slide into a hothouse climate in which water vapor radiatively

heats the lower troposphere and low-level clouds are far less common (Seeley and Wordsworth 2021). Our G3 simulations share both of these characteristics of the hothouse climate, which we intend to explore in future work. Second, Abbot (2014) used a CRM to study the behavior of clouds in a glaciated, "snowball Earth" climate. Like previous studies (Abbot et al. 2012, 2013), Abbot (2014) found a troposphere-filling layer of surface-warming clouds peaking in the tropical midtroposphere that they also likened to Sc under an inversion. In a GCM intercomparison of snowball Earth clouds, Abbot et al. (2012) found that the net CRF in the tropics of the summer hemisphere rose to 40 W m⁻², which is close to the net CRF of our G1 states. G1 states are vapor limited, and yet the G1 clouds possess similar, if not more, cloud condensate than the G2 states. Abbot et al. (Abbot et al. 2012; Abbot 2014) likewise found that cloud condensate densities in snowball states (with tropical surface temperatures around 265 K) are comparable to reference simulations of modern-day low clouds. It is unclear why condensate densities are insensitive to large changes in ambient vapor pressure and temperature, and this should be further explored. The process that supplies moisture to the cloud in Abbot (2014) is dry convection and in our study is turbulent diffusion in a deep boundary layer. If our varying-ξ experiments were carried out with an eddyresolving model, there would be no real distinction between the two. Given the similarities between the G1 clouds and these snowball Earth clouds, we speculate that this type of single-layer cloud morphology is a moisture rather than a temperature effect, and thus a symptom of the atmospheric dryness.

Separate parameterizations for large-scale condensation, eddy diffusion, and convection are necessary to run a 1D climate model. When the atmosphere is simulated at a higher resolution in a CRM, the inconsistencies between their treatment is removed because these processes are more sensibly and directly coupled. The G1-to-G2 transition coincides with a switch between diffusive and convective parameterizations and this fact is made very clear when convection is turned off. Is the G1-to-G2 transition a real feature or is it an artifact of the parameterizations? Previous work lends credibility to there being G1- and G2-like states in CRMs (Abbot 2014), but follow-up with a CRM is needed to know for sure.

The G2 and G3 states should be considered analogous to the climate states described by P15. There are important differences between this study and P15 in the behavior of the clouds at the onset of the climate transition from a cool state with two-layer clouds to a hot state with elevated, single-layer clouds. P15 varied the solar constant in the 1D model used in this study and observed a 30% increase in column albedo and 300% increase in the column cloud water between the control state and the climate transition, leading them to conclude that low clouds delay the onset of the transition by reflecting more sunlight. In our experiments increasing SVP, we find that the net CRF becomes more negative in two-layer cloud states because high clouds warm less. The properties of the low clouds, which dominate the planetary albedo, are mostly unchanged. Thus, an increase in either forcing (insolation or ξ) reduces the net CRF, but for different reasons. The explanation given for the low cloud instability in this work also differs from that given by P15. They argue that low clouds disappear because of a transient increase in the vertical gradient of moist static energy. We frame the low cloud instability in our varying- ξ experiments in terms of a larger trend in which increasing moisture causes the CBL height to decrease faster than the LCL. Ultimately, the CBL dips under the LCL and low clouds become unstable, triggering a climate transition. It may be that the CBL-LCL constraint is only relevant within the ξ parameter space. If not, this need not imply a contradiction with P15. Our explanation of the low cloud instability stems from consideration of equilibrium climate states whereas P15's explanation is deduced from a nonequilibrium perspective of the climate transition, or in other words from analyzing the specific chain of events of a simulation undergoing the climate transition. Still, future studies may wish to consider whether some variation of the CBL-LCL instability underlies the moist greenhouse transition.

Finally, an unresolved question is why the CBL height matters at the G2 to G3 climate transition, where the depth of the simulated boundary layer is best approximated as the NBL (Fig. 9a). A climate state where the NBL is deeper than the CBL is challenging to visualize, but time scales may be useful for intuition. The turnover time scale for the NBL ($\tau_{\rm nbl} = h_{\rm nbl}/u^*$) is a factor of 3 larger than that for the CBL ($\tau_{\rm cbl} = h_{\rm cbl}/w^*$) over the G2 states in RCE (not shown). It may be that faster mixing in the CBL is important to the formation and maintenance of low clouds in high ξ states. This hypothesis should be tested in future work.

6. Conclusions

Our primary goal was to find climate "regime transitions" for hypothetical planets with vapor-rich and vapor-poor atmospheres. We did this parametrically through a multiplicative constant, ξ , on the SVP of water at each temperature. Although motivated by "end-member" climate states on Earth and Titan, our focus necessarily involved extrapolation of the thermodynamics of the natural world through the alteration of the SVP of water. We also chose to restrict this study to a 1D climate model, which is well behind the state-of-the-art. This approach allows a broad study of ξ , providing testable hypotheses for future studies with a CRM. This abstraction, while clearly artificial, is nonetheless necessary to achieve our goal.

We put forward four hypotheses for the effects of changing the moisture content of an atmospheric column on clouds: 1) high clouds get higher as SVP increases, 2) low clouds get lower as SVP increases, 3) some vapor-poor states have a single cloud layer, and 4) some vapor-rich states have a single cloud layer. We tested the hypotheses with numerical experiments in which the SVP of water was artificially altered by a constant, ξ , in a single-column climate model. By altering the volatility of water vapor on an aquaplanet with Earth's background atmospheric composition, we isolated multiple effects of moisture on climate, clouds, and convection (CCC). These effects are illustrated in Fig. 16. Below, we enumerate the main conclusions.

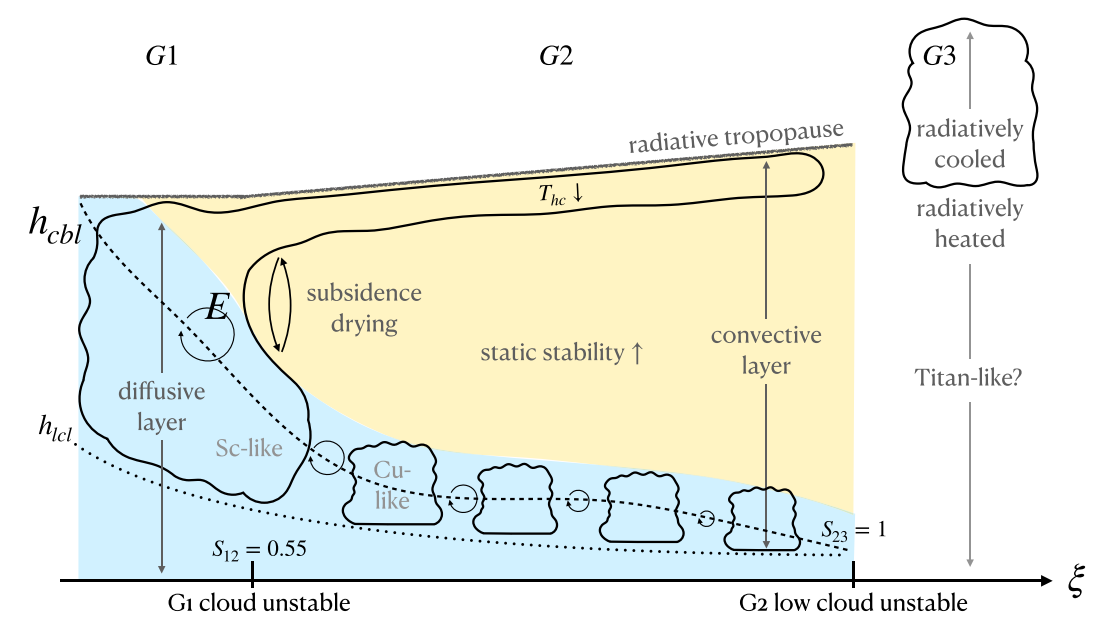


FIG. 16. Illustration of the effect of varying ξ on climate, clouds, and convection. $h_{\rm cbl}$ is the height of the convective boundary layer and is traced as a dashed black line. $h_{\rm lcl}$ is the lifting condensation level and is traced as a dotted black line. Entrainment of free tropospheric air into the boundary layer (i.e., E) is depicted as a circular arrow. $T_{\rm hc}$ is the high cloud temperature. S_{12} and S_{23} are the cloud instability parameters referenced in the text that describe the $G1 \rightarrow G2$ and $G2 \rightarrow G3$ climate transitions, respectively. Clouds are sketched as thick, enclosed curves. Subsidence is depicted as a pair of ascending and descending arrows. The diffusive and convective mixing layers are represented by blue and yellow shading, respectively. Shading preference is given to the former anywhere the two layers overlap.

- 1) Three cloudy climate states are found by varying ξ . Earth-like, intermediate ξ states (G2) with 0.4–2 cm of precipitable water are in RCE, the surface temperature and column-integrated relative humidity are roughly constant, and clouds in the lower and upper troposphere with a net cooling effect are separated by a dry, cloud-free layer. In low ξ states (G1) with 0.1–0.3 cm of precipitable water, a single cloud layer warms the surface by as much as 25 K relative to the reference state (ξ = 1). High ξ states (G3) have a surface temperature of 360 K, 5 m of precipitable water, and a radiatively heated lower troposphere overlain by a radiatively cooled upper troposphere with a single, net-cooling cloud.
- 2) High clouds get higher because they are bound by radiative constraints to occur at a lower temperature as ξ increases. For G2 states in RCE, the anvil cloud maximum and clear-sky longwave cooling decreases at a roughly constant vapor pressure path (VPP) predicted by an analytical theory of radiative transfer (JF20b). This result is perhaps the clearest demonstration of the FAT hypothesis to date.
- 3) Low clouds get lower because they are coupled to the convective boundary layer (CBL), which shallows with increasing ξ. The CBL shallows because of a partial cancellation between increased tropospheric stability and a reduced convective area fraction. The increase in tropospheric stability is due to a decrease in the lapse rate of the free troposphere, which causes the vertical gradient in potential temperature to increase. The convective area fraction change

- reflects that fewer positively buoyant surface eddies reach the mean-state LCL as ξ increases.
- 4) Two-layer clouds first appear in vapor-poor states when a shallowing diffusively mixed layer (with increasing ξ) separates from a convectively mixed layer that tops out at the tropopause. Above the diffusive layer, moist convection maintains a thin high cloud (G2). Subsidence drying produces a relative humidity minimum at the separation level. The diffusively mixed layer maintains the G2 low cloud. Clouds are well-separated in G2 because of the vertical offset of the diffusively mixed layer and the level of deep convective detrainment.
- 5) G1 to G2 is an atypical Sc-to-Cu transition. At the transition, the G1 cloud meets the minimum set of requirements for an Sc deck to decouple from the surface. Decoupling is primarily driven by a quasi-linear dependence of the surface latent heat flux on ξ. Across the transition, there is a 40% drop in peak cloud fraction and a 5 K drop in surface temperature.
- 6) Low clouds break up at the climate transition from G2 to G3 when the convective boundary layer falls below the lifting condensation level, cutting off the supply of moisture from the surface to the cloud. We combine the relevant physics into an instability parameter S₂₃ that describes this constraint on low cloud formation and contextualizes the climate transition.

Our main conclusions are drawn from a single climate model and need to be reproduced with another 1D model, or better yet, a CRM to be confident in their robustness. Although Titan, Saturn's largest moon, motivates the exploration of climate states with extreme levels of moisture (relative to Earth), our main findings have limited applicability to Titan itself. As measured by moisture content, G3 states are the most Titan-like. Further study of G3 may offer insight into effect of enhanced moisture on climate, clouds, and convection.

Acknowledgments. This work was supported by NSF Grant 1912673 and an Early-Career Fellowship from the Center for Diverse Leadership in Science at UCLA. We thank Max Popp for sharing the modified climate model and his expertise at several stages of this work. We thank Ben Winjum and Sebastian Rast for technical support and three anonymous reviewers whose comments improved the manuscript.

Data availability statement. Simulations with the ECHAM6 climate model were carried out on UCLA's Hoffman2 Cluster. The data from this study are archived at 10.5281/zenodo. 7814685.

REFERENCES

- Abbot, D. S., 2014: Resolved snowball Earth clouds. *J. Climate*, **27**, 4391–4402, https://doi.org/10.1175/JCLI-D-13-00738.1.
- —, A. Voigt, M. Branson, R. T. Pierrehumbert, D. Pollard, G. Le Hir, and D. D. B. Koll, 2012: Clouds and snowball Earth deglaciation. *Geophys. Res. Lett.*, 39, L20711, https://doi.org/10.1029/2012GL052861.
- —, —, D. Li, G. L. Hir, R. T. Pierrehumbert, M. Branson, D. Pollard, and D. D. Daniel, 2013: Robust elements of snowball Earth atmospheric circulation and oases for life. *J. Geophys. Res. Atmos.*, 118, 6017–6027, https://doi.org/10.1002/jgrd.50540.
- Albrecht, B., and Coauthors, 2019: Cloud System Evolution in the Trades (CSET): Following the evolution of boundary layer cloud systems with the NSF-NCAR GV. *Bull. Amer. Meteor. Soc.*, 100, 93–121, https://doi.org/10.1175/BAMS-D-17-0180.1.
- Arya, S. P., 1988: Momentum and heat exchanges with homogeneous surfaces. *Introduction to Micrometeorology*, S. P. Arya, Ed., International Geophysics Series, Vol. 42, Academic Press, 157–181, https://doi.org/10.1016/S0074-6142(08)60426-X.
- Bretherton, C. S., and M. C. Wyant, 1997: Moisture transport, lower-tropospheric stability, and decoupling of cloud-topped boundary layers. *J. Atmos. Sci.*, 54, 148–167, https://doi.org/10.1175/1520-0469(1997)054<0148:MTLTSA>2.0.CO;2.
- —, P. N. Blossey, and C. R. Jones, 2013: Mechanisms of marine low cloud sensitivity to idealized climate perturbations: A single-LES exploration extending the CGILS cases. *J. Adv. Model. Earth Syst.*, 5, 316–337, https://doi.org/10.1002/jame. 20019.
- Caballero, R., and M. Huber, 2010: Spontaneous transition to superrotation in warm climates simulated by CAM3. *Geophys. Res. Lett.*, 37, L11701, https://doi.org/10.1029/2010GL043468.
- Cesana, G., A. D. Del Genio, and H. Chepfer, 2019: The Cumulus And Stratocumulus CloudSat-CALIPSO Dataset (CASC-CAD). Earth Syst. Sci. Data, 11, 1745–1764, https://doi.org/10. 5194/essd-11-1745-2019.
- Cuijpers, J. W. M., and P. G. Duynkerke, 1993: Large eddy simulation of trade wind cumulus clouds. J. Atmos. Sci., 50,

- 3894–3908, https://doi.org/10.1175/1520-0469(1993)050<3894: LESOTW>2.0.CO;2.
- —, and P. Bechtold, 1995: A simple parameterization of cloud water related variables for use in boundary layer models. *J. Atmos. Sci.*, **52**, 2486–2490, https://doi.org/10.1175/1520-0469 (1995)052<2486:ASPOCW>2.0.CO;2.
- Deardorff, J. W., 1972: Parameterization of the planetary boundary layer for use in general circulation models. *Mon. Wea. Rev.*, **100**, 93–106, https://doi.org/10.1175/1520-0493(1972)100 <0093:POTPBL>2.3.CO;2.
- Driedonks, A. G. M., and H. Tennekes, 1984: Entrainment effects in the well-mixed atmospheric boundary layer. *Bound.-Layer Meteor.*, 30, 75–105, https://doi.org/10.1007/BF00121950.
- Frierson, D. M. W., I. M. Held, and P. Zurita-Gotor, 2006: A gray-radiation aquaplanet moist GCM. Part I: Static stability and eddy scale. J. Atmos. Sci., 63, 2548–2566, https://doi.org/ 10.1175/JAS3753.1.
- —, —, and —, 2007: A gray-radiation aquaplanet moist GCM. Part II: Energy transports in altered climates. *J. Atmos. Sci.*, **64**, 1680–1693, https://doi.org/10.1175/JAS3913.1.
- Giorgetta, M. A., and Coauthors, 2013: The atmospheric general circulation model ECHAM6: Model description. MPI Rep. on Earth System Science 135, 177 pp., https://pure.mpg.de/ rest/items/item_1810480_15/component/file_1810481/content.
- Griffith, C. A., J. L. Hall, and T. R. Geballe, 2000: Detection of daily clouds on Titan. *Science*, 290, 509–513, https://doi.org/ 10.1126/science.290.5491.509.
- Harrop, B. E., and D. L. Hartmann, 2012: Testing the role of radiation in determining tropical cloud-top temperature. *J. Climate*, 25, 5731–5747, https://doi.org/10.1175/JCLI-D-11-00445.1.
- Hartmann, D. L., 2016: Global Physical Climatology. Elsevier, 325–360, https://doi.org/10.1016/C2009-0-00030-0.
- —, and K. Larson, 2002: An important constraint on tropical cloud-climate feedback. *Geophys. Res. Lett.*, 29, 1951, https:// doi.org/10.1029/2002GL015835.
- ——, B. D. Dygert, P. N. Blossey, Q. Fu, and A. B. Sokol, 2022: The vertical profile of radiative cooling and lapse rate in a warming climate. *J. Climate*, 35, 2653–2665, https://doi.org/10. 1175/JCLI-D-21-0861.1.
- Iacono, M. J., J. S. Delamere, E. J. Mlawer, M. W. Shephard, S. A. Clough, and W. D. Collins, 2008: Radiative forcing by long-lived greenhouse gases: Calculations with the AER radiative transfer models. *J. Geophys. Res.*, 113, D13103, https:// doi.org/10.1029/2008JD009944.
- Jeevanjee, N., and S. Fueglistaler, 2020: Simple spectral models for atmospheric radiative cooling. *J. Atmos. Sci.*, 77, 479–497, https://doi.org/10.1175/JAS-D-18-0347.1.
- Johnson, R. H., T. M. Rickenbach, S. A. Rutledge, P. E. Ciesielski, and W. H. Schubert, 1999: Trimodal characteristics of tropical convection. *J. Climate*, 12, 2397–2418, https://doi.org/10.1175/1520-0442(1999)012<2397:TCOTC>2.0.CO;2.
- King, M. D., S. Platnick, W. P. Menzel, S. A. Ackerman, and P. A. Hubanks, 2013: Spatial and temporal distribution of clouds observed by MODIS onboard the Terra and Aqua satellites. *IEEE Trans. Geosci. Remote Sens.*, 51, 3826–3852, https://doi.org/10.1109/TGRS.2012.2227333.
- Leconte, J., F. Forget, B. Charnay, R. Wordsworth, and A. Pottier, 2013: Increased insolation threshold for runaway greenhouse processes on Earth-like planets. *Nature*, 504, 268–271, https://doi.org/10.1038/nature12827.
- Lora, J. M., J. I. Lunine, and J. L. Russell, 2015: GCM simulations of Titan's middle and lower atmosphere and comparison to

- observations. *Icarus*, **250**, 516–528, https://doi.org/10.1016/j.icarus.2014.12.030.
- Lorenz, R. D., C. A. Griffith, J. I. Lunine, C. P. McKay, and N. O. Rennò, 2005: Convective plumes and the scarcity of Titan's clouds. *Geophys. Res. Lett.*, 32, L01201, https://doi.org/ 10.1029/2004GL021415.
- Mauritsen, T., and Coauthors, 2012: Tuning the climate of a global model. *J. Adv. Model. Earth Syst.*, **4**, M00A01, https://doi.org/10.1029/2012MS000154.
- Mitchell, J. L., and J. M. Lora, 2016: The climate of Titan. Annu. Rev. Earth Planet. Sci., 44, 353–380, https://doi.org/10.1146/annurev-earth-060115-012428.
- Möbis, B., and B. Stevens, 2012: Factors controlling the position of the intertropical convergence zone on an aquaplanet. *J. Adv. Model. Earth Syst.*, 4, M00A04, https://doi.org/10.1029/ 2012MS000199.
- Neggers, R., B. Stevens, and J. D. Neelin, 2006: A simple equilibrium model for shallow-cumulus-topped mixed layers. *Theor. Comput. Fluid Dyn.*, 20, 305–322, https://doi.org/10.1007/s00162-006-0030-1.
- —, and —, 2007: Variance scaling in shallow-cumulus-topped mixed layers. *Quart. J. Roy. Meteor. Soc.*, **133**, 1629–1641, https://doi.org/10.1002/qj.105.
- O'Gorman, P. A., R. P. Allan, M. P. Byrne, and M. Previdi, 2012: Energetic constraints on precipitation under climate change. Surv. Geophys., 33, 585–608, https://doi.org/10.1007/s10712-011-9159-6.
- Popp, M., H. Schmidt, and J. Marotzke, 2015: Initiation of a runaway greenhouse in a cloudy column. *J. Atmos. Sci.*, **72**, 452– 471, https://doi.org/10.1175/JAS-D-13-047.1.
- —, and —, 2016: Transition to a moist greenhouse with CO₂ and solar forcing. *Nat. Commun.*, **7**, 10627, https://doi.org/10.1038/ncomms10627.
- Rafkin, S. C. R., J. M. Lora, A. Soto, and J. M. Battalio, 2022: The interaction of deep convection with the general circulation in Titan's atmosphere. Part 1: Cloud resolving simulations. *Icarus*, 373, 114755, https://doi.org/10.1016/j.icarus.2021. 114755.
- Rieck, M., L. Nuijens, and B. Stevens, 2012: Marine boundary layer cloud feedbacks in a constant relative humidity atmosphere. J. Atmos. Sci., 69, 2538–2550, https://doi.org/10.1175/ JAS-D-11-0203.1.
- Romps, D. M., 2014: An analytical model for tropical relative humidity. J. Climate, 27, 7432–7449, https://doi.org/10.1175/ JCLI-D-14-00255.1.
- ——, 2017: Exact expression for the lifting condensation level. J. Atmos. Sci., 74, 3891–3900, https://doi.org/10.1175/JAS-D-17-0102.1.
- Sassen, K., and Z. Wang, 2008: Classifying clouds around the globe with the CloudSat radar: 1-year of results. *Geophys. Res. Lett.*, 35, L04805, https://doi.org/10.1029/2007GL032591.
- —, and D. Liu, 2009: Cirrus clouds and deep convection in the tropics: Insights from CALIPSO and CloudSat. *J. Geophys. Res.*, **114**, D00H06, https://doi.org/10.1029/2009JD011916.

- Schneider, T., C. M. Kaul, and K. G. Pressel, 2019: Possible climate transitions from breakup of stratocumulus decks under greenhouse warming. *Nat. Geosci.*, 12, 163–167, https://doi.org/10.1038/s41561-019-0310-1.
- Seeley, J. T., and R. D. Wordsworth, 2021: Episodic deluges in simulated hothouse climates. *Nature*, 599, 74–79, https://doi. org/10.1038/s41586-021-03919-z.
- —, N. Jeevanjee, W. Langhans, and D. M. Romps, 2019a: Formation of tropical anvil clouds by slow evaporation. *Geophys. Res. Lett.*, 46, 492–501, https://doi.org/10.1029/2018GL080747.
- —, and D. M. Romps, 2019b: FAT or FiTT: Are anvil clouds or the tropopause temperature invariant? *Geophys. Res. Lett.*, **46**, 1842–1850, https://doi.org/10.1029/2018GL080096.
- Slingo, J. M., 1980: A cloud parametrization scheme derived from GATE data for use with a numerical model. *Quart. J. Roy. Meteor. Soc.*, 106, 747–770, https://doi.org/10.1002/qj.49710645008.
- Sokol, A. B., and D. L. Hartmann, 2020: Tropical anvil clouds: Radiative driving toward a preferred state. *J. Geophys. Res. Atmos.*, 125, e2020JD033107, https://doi.org/10.1029/2020JD033107.
- Stevens, B., 2006: Bulk boundary-layer concepts for simplified models of tropical dynamics. *Theor. Comput. Fluid Dyn.*, 20, 279–304, https://doi.org/10.1007/s00162-006-0032-z.
- —, and Coauthors, 2013: Atmospheric component of the MPI-M Earth system model: ECHAM6. J. Adv. Model. Earth Syst., 5, 146–172, https://doi.org/10.1002/jame.20015.
- Stull, R. B., 1988: An Introduction to Boundary Layer Meteorology. Kluwer Academic, 666 pp.
- Sundqvist, H., E. Berge, and J. E. Kristjánsson, 1989: Condensation and cloud parameterization studies with a mesoscale numerical weather prediction model. *Mon. Wea. Rev.*, 117, 1641–1657, https://doi.org/10.1175/1520-0493(1989)117<1641: CACPSW>2.0.CO;2.
- Tan, Z., T. Schneider, J. Teixeira, and K. G. Pressel, 2017: Large-eddy simulation of subtropical cloud-topped boundary layers:

 Cloud response to climate change. J. Adv. Model. Earth Syst., 9, 19–38, https://doi.org/10.1002/2016MS000804.
- Tiedtke, M., 1989: A comprehensive mass flux scheme for cumulus parameterization in large-scale models. *Mon. Wea. Rev.*, **117**, 1779–1800, https://doi.org/10.1175/1520-0493(1989)117 <1779:ACMFSF>2.0.CO:2.
- Tokano, T., C. P. McKay, F. M. Neubauer, S. K. Atreya, F. Ferri, M. Fulchignoni, and H. B. Niemann, 2006: Methane drizzle on Titan. *Nature*, 442, 432–435, https://doi.org/10.1038/nature04948.
- Wolf, E. T., and O. B. Toon, 2015: The evolution of habitable climates under the brightening sun. J. Geophys. Res. Atmos., 120, 5775–5794, https://doi.org/10.1002/2015JD023302.
- Wood, R., 2012: Stratocumulus clouds. Mon. Wea. Rev., 140, 2373–2423, https://doi.org/10.1175/MWR-D-11-00121.1.
- —, and C. S. Bretherton, 2006: On the relationship between stratiform low cloud cover and lower-tropospheric stability. *J. Climate*, 19, 6425–6432, https://doi.org/10.1175/JCLI3988.1.
- Yang, D., and S. D. Seidel, 2020: The incredible lightness of water vapor. J. Climate, 33, 2841–2851, https://doi.org/10.1175/JCLI-D-19-0260.1.